J. Fluid Mech. (2009), *vol.* 621, *pp.* 23–57.
doi:10.1017/S0022112008004813 Printed in the United Kingdom

Direct numerical simulation of turbulence in a square annular duct

HONGYI XU†

Institute for Aerospace Research, National Research Council, Ottawa, ON, Canada

(Received 7 November 2007 and in revised form 26 August 2008)

Direct numerical simulation (DNS) is performed to investigate the fully developed turbulence in a straight square annular duct. The mean flow field and the turbulent statistics are compared with existing experiments and numerical results. The comparisons and the analysis of the DNS data led to the discovery of the turbulent boundary layers of concave and convex 90° corners, a corner flow similarity and the scaling characteristics of corner turbulence. Analysis of the mean streamwise velocity near the concave and convex 90° corners resulted in establishing the 'law-of-the-corner' formulations. Comparing these formulations with the 'law-of-the-wall' relation, both damping and enhancing mechanisms analytically represented by the van Driest damping function, and the enhancement function were revealed for the concave and convex corner turbulence. The investigation captures the distinctive turbulence-driven secondary flows for both convex and concave 90° corners, and a corner flow similarity rule is discovered, which is associated with the pattern of these secondary flows. A turbulence energy spectrum analysis provides the distinctive features of the fully developed turbulence in the wall and corner regions. The validity of the turbulence eddy viscosity concept is evaluated based on these turbulence energy spectra. The turbulence-driven secondary-flow generation mechanisms are investigated by analysing the anisotropy of the Reynolds stresses.

1. Introduction

Turbulent flows in pipes or channels (internal flows) and the turbulent boundary layer on a flat plate or an airfoil (external flows) have been intensively investigated over the last century, ever since Reynolds (1883) first found turbulent flow in a circular pipe and Prandtl (1904) first put forward the boundary-layer theory for flows past flat plates and circular cylinders. However, the investigations of turbulence in the vicinity of a streamwise corner are relatively scarce because it was difficult to make any flow simplifications in early analytical methods, and modern numerical simulation technologies (both hardware and software) were not powerful and advanced enough to directly attack these problems. The CPU speed and the RAM memory size were the main limitations on the hardware side, while the large eddy simulation (LES)/direct numerical simulation (DNS) solution techniques, particularly the fast Poisson solver technique (see Wesseling 2001) were the major constraints on the software side. The earliest attempt to address the turbulence near streamwise corners can be dated back to Prandtl (1926) in which the origins of the flow perpendicular to the streamwise direction in a generic duct were identified as pressure-driven secondary

† Email address for correspondence: hongyi.xu@nrc.ca

flows and turbulence-driven secondary flows (TDSFs). As elaborated in Bradshaw (1987), two distinct mechanisms were found responsible for generating secondary flows: skew-induced vortex generation by quasi-inviscid deflections of the mean vorticity and stress-induced vortex generation by anisotropy and inhomogeneous turbulence (Reynolds) stresses. The stress-induced mechanism produces a TDSF in a generic straight duct, well-known as Prandtl's second kind of secondary flow. Nikuradse (1930) first experimentally investigated the fully developed turbulence inside a straight square duct and observed a TDSF as a distinctive counter-rotating vortex pair symmetrically located around the bisector of the concave 90° corner.

Numerical simulations have been applied to the turbulent flow in a square duct over the last three decades. Earlier Reynolds-averaged Navier–Stokes (RANS) methods with conventional closure models based on isotropy assumptions, such as the conventional $k-\varepsilon$ and $k-\omega$ models, failed to predict any TDSF. Launder & Ying (1973) and Speziale (1987) developed an algebraic stress model and a nonlinear $k-\varepsilon$ model, respectively, to address the anisotropy in the Reynolds stresses and were successful in qualitatively capturing the TDSF when applied to a square duct. Demuren & Rodi (1984) provided a comprehensive review of the progress of capturing the TDSF, using experiments and RANS simulations in that period of time.

The progress of computer technology in the 1990s made it possible to perform LES and DNS for simple geometry flows, such as channel flows and square duct flows. LES of square duct flows at this period of time can be found in Madabhushi & Vanka (1991), Kajishima & Miyake (1992) and Breuer & Rodi (1994). Examples of DNS of turbulence in a square duct include Gavrilakis (1992) and Huser & Biringen (1993). These results were compared with the results of a variety of experiments, such as Niederschulte (1989), Nishino & Kasagi (1989), Kreplin & Eckelmann (1979), Alfredsson *et al.* (1988) and Cheesewright, McGrath & Petty (1990). Reasonable agreements were obtained for the mean flow and turbulence statistics.

As computing hardware technologies, particularly RAM size and CPU speed, advanced to the point at which it permitted LES or DNS to attack turbulence at moderately high Reynolds numbers for medium-complexity flow geometries, Xu & Pollard (2001) first investigated the turbulence in a square annular duct (see figure 1) using LES. The simulation was validated by comparing the results with the DNSs from Gavrilakis (1992) and Huser & Biringen (1993) and the universal 'law-of-the-wall' in von Karman (1930). Important discoveries of this LES research included (1) the prediction of the pattern of the TDSF near the convex 90° corner and (2) the extension of the boundary-layer concept and analysis to the streamwise corner flows. The streamwise velocity along corner bisector was plotted on a logarithmic scale to quantitatively study the effects of the TDSF of a corner boundary layer. The preliminary 'law-of-the-corner' formulations for the concave and convex 90° corners were derived. The grid resolution and density near the convex 90° corner was found insufficient.

To advance the LES research in Xu & Pollard (2001), a DNS is conducted to further resolve the turbulence in a square annular duct, particularly the turbulent boundary layer of the concave and convex 90° corners. The Navier–Stokes (N-S) solution method in the current study is based on the flexible-cycle additive-correction multigrid (FCAC-MG) technique in Xu, Yuan & Khalid (2005). The development of a high-performance Poisson solver and the discovery of the solvability condition for the Poisson equation with periodic velocity boundary conditions made it possible to drive the residual of the discretized equations down to the computer round-off error, which guarantees that a strong conservation of the mass and momentum be completely satisfied. The TDSF (Prandtl's second kind) is accurately captured for the concave and

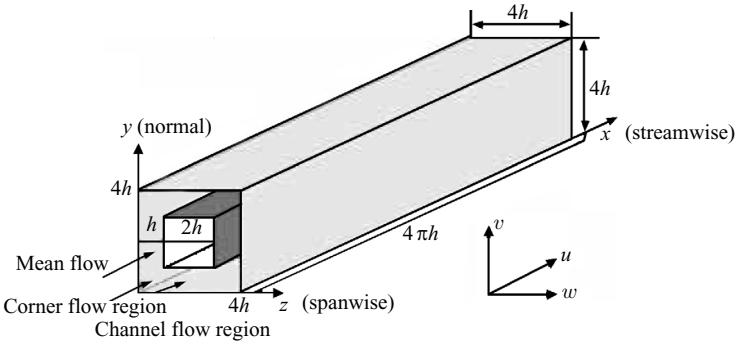

FIGURE 1. Square annular duct flow configuration.

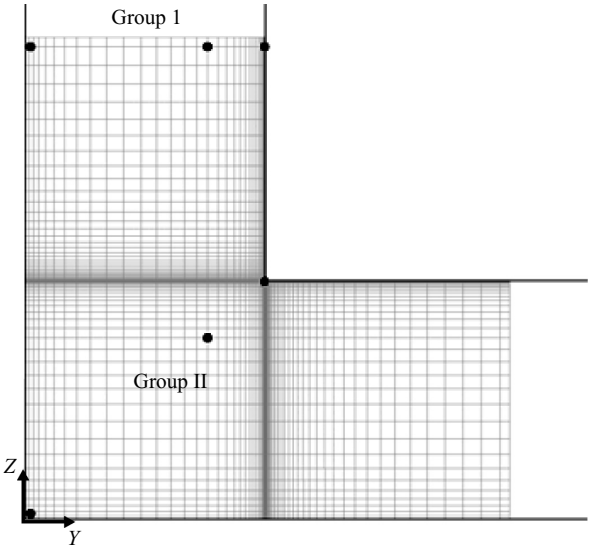

FIGURE 2. Sampling points on the cross-section of the square annular duct in which the TES were calculated.

convex 90° corners. The turbulence energy spectra (TES) were obtained on a number of sampling points (see figure 2) and were benchmarked by the Kolmogorov (1962) law. Compared with the previous LES, the current DNS yields better agreements with the 'law-of-the-wall' relationship and the other DNS results. 'Law-of-the-corner' formulations are derived along the corner bisector for both concave and convex 90° corners. These formulations are found closely dependent on the patterns of the TDSF, and the rules are laid out to determine the corner formulations for other generic concave or convex corners. A flow similarity is discovered for the concave 90° corner by comparing the data with the DNS from Gavrilakis (1992) and the experiment from Cheesewright *et al.* (1990). The TES analysis reveals some distinctive features of turbulence anisotropic motions in near-wall, near-corner and homogeneous flow regimes, which leads to the re-evaluation of the validity of the conventional turbulence eddy viscosity as proposed by Kolmogorov (1942). Turbulence statistics (Reynolds stresses) are obtained, and their anisotropy properties are directly interrogated to better understand the origins of the TDSF.

2. Physical model and computations

2.1. *Governing equations*

Following the same problem-scaling procedure as in Xu & Pollard (2001), the governing equations in the current DNS are the incompressible unsteady N-S equations, mathematically representing the conservation laws of mass and momentum:

$$\frac{\partial u_i}{\partial x_i} = 0 \tag{2.1}$$

$$\frac{\partial u_i}{\partial t} + \frac{\partial u_j u_i}{\partial x_j} = -\frac{\partial p}{\partial x_i} + 2\delta_{1i} + \frac{1}{\mathrm{Re}_\tau}\left[\frac{\partial}{\partial x_j}\left(\frac{\partial u_i}{\partial x_j} + \frac{\partial u_j}{\partial x_i}\right)\right], \tag{2.2}$$

where the indices $i, j, k = 1, 2, 3$ refer to the x, y and z directions; x is the streamwise direction, and y and z are the transverse directions; $2\delta_{1i}$ represents streamwise mean pressure gradient.

For reference, these abbreviations are used in the following figure legends: EXP experiment; SQD square duct; AND annular duct; RTC rectangular channel; PLC plane channel; WBS wall bisector; CBS corner bisector; CCC concave 90° corner; CVC convex 90° corner; INW inner wall (of the inner duct); OTW outer wall (of the outer duct).

2.2. *Simulation set-up*

In the cross-streamwise directions, the grid density (number of grid points) was increased by a factor of two in each direction compared with the LES grid in Xu & Pollard (2001). Based on the analysis of the streamwise velocity near the wall and corners (see figure 16*a*, *b* in Xu & Pollard 2001) the grid resolutions, measured by the $y^+ = yu_\tau/\nu$ or $d_n^+ = d_n u_\tau/\nu$ of the first point away from the wall or corner, and the grid densities in the boundary layers of the inner and outer walls were reset and redistributed to suit the need for better resolving the flow. As shown in Xu & Pollard (2001), the streamwise velocity was under-resolved near the convex corner; the d_n^+ value must be well below one to resolve the convex-corner inner boundary layer. Therefore, the DNS grid resolution was increased significantly in the region by reducing the minimum y^+ or d_n^+ value from 1.259 in the LES to 0.195 in the DNS. The grid density near the inner wall and convex corner was increased from 14 points in the LES to 39 in the DNS. The strong dampening effect of a concave corner on the streamwise velocity (see Xu & Pollard 2001) produced a thicker concave-corner boundary layer than the one on a flat plate. Therefore, the grid resolution near the outer wall and concave corner was slightly changed from $y^+ = 1.294$ in the LES to $y^+ = 0.724$ in the DNS and the grid density near the concave 90° corner was slightly increased from 20 points in the LES to 27 in the DNS.

In the streamwise direction, the grids were uniform, and the grid density was almost doubled from 130 in the LES to 256 in the DNS. According to Huser & Biringen (1993), the non-dimensional length of the square duct was set at 2π, using the hydraulic diameter as the characteristic length, which was sufficient to resolve the most anisotropic turbulence eddies near the concave corner. Since the anisotropy of turbulence eddy near a convex 90° corner was not stronger than that near a concave 90° corner, an equivalent length of 4π, with half of the hydraulic diameter of the square annular duct being the characteristic length, was selected, giving a grid resolution of $\Delta x^+ = 9.973$ in the streamwise direction. Two groups of sampling points in figure 2, Group I along the wall bisector and Group II along the corner bisector, were placed on the cross-section plane in which the TES were calculated.

Run	Grid	T_{tot}	Δt	Δy_i^+,	Δy_o^+	Δx^+	Re_τ	Re_b	Domain
DNS	$256 \times 258 \times 258$	9	1.0×10^{-4}	0.195,	0.724	9.973	200	3058	$4\pi \times 4 \times 4$
LES	$130 \times 130 \times 130$	10	2.5×10^{-4}	1.259,	1.294	39.58	200	3349	$8\pi \times 4 \times 4$

TABLE 1. Computational parameters for the LES and DNS runs.

The initial conditions were generated by interpolating an instantaneous LES solution in Xu & Pollard (2001) onto the DNS grid. Because of the increase in the grid density and resolution, the non-dimensional time step in the DNS was reduced from 2.5×10^{-4} to 1.0×10^{-4} to satisfy the Courant–Friedrich–Levy condition (CFL) number restriction: CFL < 0.5. The simulation was performed at a Reynolds number of 200 based on the mean frictional velocity u_τ and half the hydraulic diameter of the square annular duct (equivalent to h in figure 1). One large eddy turnover time (LETOT $= h/u_\tau$), or 10 000 time steps, was used to get rid of the transition effects from the LES to the DNS, and then the turbulence statistics were accumulated over nine LETOTs, or 90 000 time steps. Table 1 summarizes the key computational parameters compared with the ones in the LES study. The total sampling time T_{tot} and the time step Δt are normalized by LETOT. The Reynolds numbers, Re_τ and Re_b, are defined as $Re_\tau = u_\tau h/\nu$ and $Re_b = u_b h/\nu$, respectively.

2.3. *Numerical techniques*

The N-S equations were spatially discretized using a second-order finite-volume method on a staggered grid. The temporal discretization was effected through the second-order Adams–Bashforth scheme for the convection terms and the second-order Adams–Moulton scheme for the diffusion terms. The fractional step method in Kim & Moin (1985) was applied to obtain a time-dependent pressure and divergence-free velocity. The solution techniques for the discretized N-S equations was based on the conventional and modified tri-diagonal matrix algorithms (TDMAs) coupled with an FCAC-MG technique in Xu *et al.* (2005).

3. Analysis of the DNS results

Code validation and a detailed analysis of the LES results were reported in Xu & Pollard (2001). The current DNS aims to completely resolve the turbulence inside a square annular duct and further reveal new features of turbulence physics near the corner regions. The statistics, including the mean flow field, the Reynolds stresses and the TES, were obtained by averaging the accumulations over a period of nine LETOTs. The quality of these statistics was further improved via averaging the accumulations in the homogeneous direction and conducting the quadrant and triangle averagings due to the geometrical symmetry properties, as suggested by Gavrilakis (1992) and Huser & Biringen (1993).

3.1. *Mean flow field*

3.1.1. *Overview of the mean flow field*

The current DNS predicted a bulk mean streamwise velocity of $U_b^+ = 15.28$, which gave a friction factor of $f = 8u_\tau^2/U_b^2 = 0.034$, close to the one for a rectangular duct (0.030) in Hartnett, Koh & McComas (1962). The slight increase is attributed to the convex corner that causes a sharp increase in the local wall shear stress (see § 3.1.3). The DNSs from Gavrilakis (1992) and Huser & Biringen (1993) yielded friction

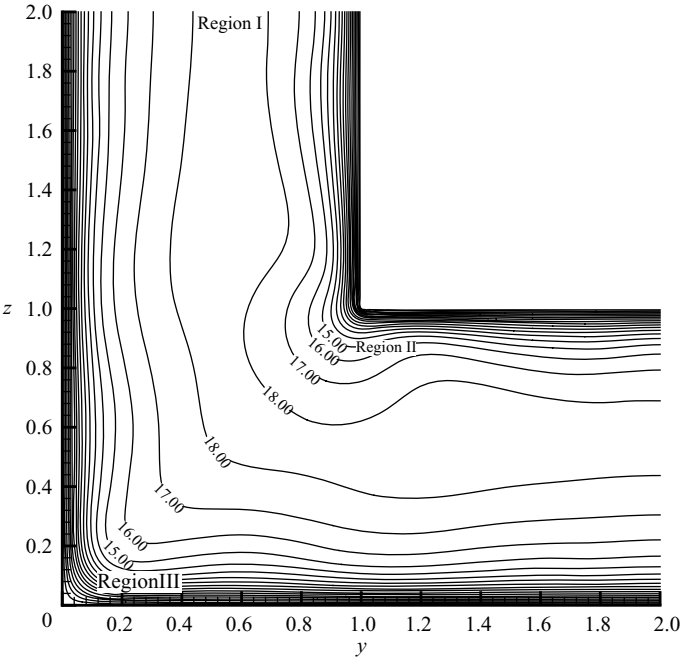

FIGURE 3. Mean streamwise velocity contours in the lower-left quadrant of the square annular duct.

factors of $f = 0.037$ and $f = 0.027$, respectively. The maximum mean streamwise velocity was $U_0^+ = 18.69$ located at $(y, z) = (1.349, 0.575)$ on the cross-streamwise plane. Therefore, the ratio of the maximum to bulk velocity was $U_0/U_b = 1.22$. Figures 3 and 4(a) present the mean streamwise velocity contours and the mean TDSF vectors, respectively, for the lower-left quadrant of the square annular duct. Figure 4(b) details the mean TDSF near the convex corner. The contours near the wall bisector (Region I) are fairly flat, indicating that the flow is almost parallel to the inner and outer walls, close to the scenario of a channel flow. The contours in figure 3 clearly identify a bulge away from the convex corner of the inner square duct (Region II) and a bulge towards the concave corner of the outer square duct (Region III). Following the argument in Nikuradse (1930), these bulges imply the existence of TDSFs pointing away from the convex corner and directed towards the concave corner. The vector plots of the mean TDSF in figure 4(a, b) confirm the conjecture by exhibiting the counter-rotating vortex pairs, located symmetrically around both the convex and concave corners. The vortex pair near the concave corner of the outer square duct is reminiscent of the vortex structure in a square duct, while the TDSF vortex structure near the convex corner is comparable to the ones in the vicinity of a riblet peak predicted by Choi, Moin & Kim (1993).

The streamwise mean velocity U^+ scaled by the mean frictional velocity u_τ is compared to the square duct DNS and the previous LES for a square annular duct (see figure 5a, b). The comparisons are provided along the wall bisector (Region I) and the corner bisector (Regions II and III), with the horizontal axes normalized by the wall bisector distance and the diagonal distance, respectively. The obvious grid dependence of LES solution manifests the necessity to conduct a DNS to eliminate the coarse-grid diffusion effect that tends to overpredict U^+.

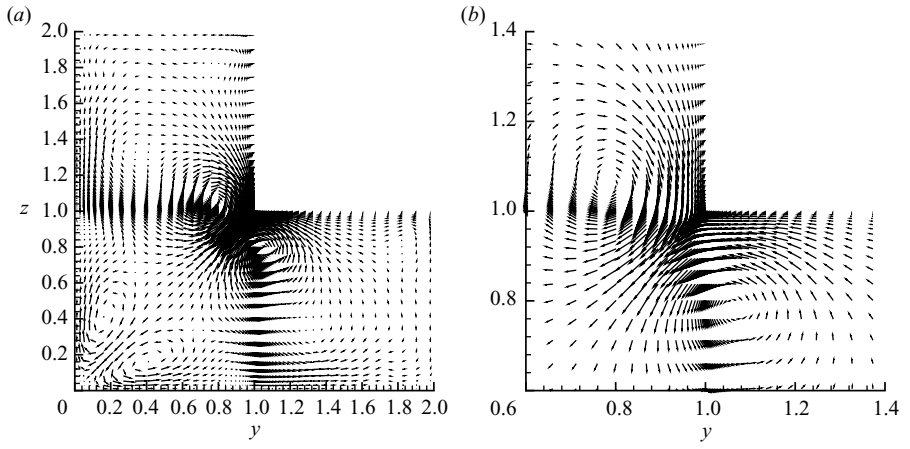

FIGURE 4. Mean turbulence-driven secondary velocity vectors in the lower-left quadrant of square annular duct: (*a*) entire quadrant and (*b*) enlarged view near the convex corner.

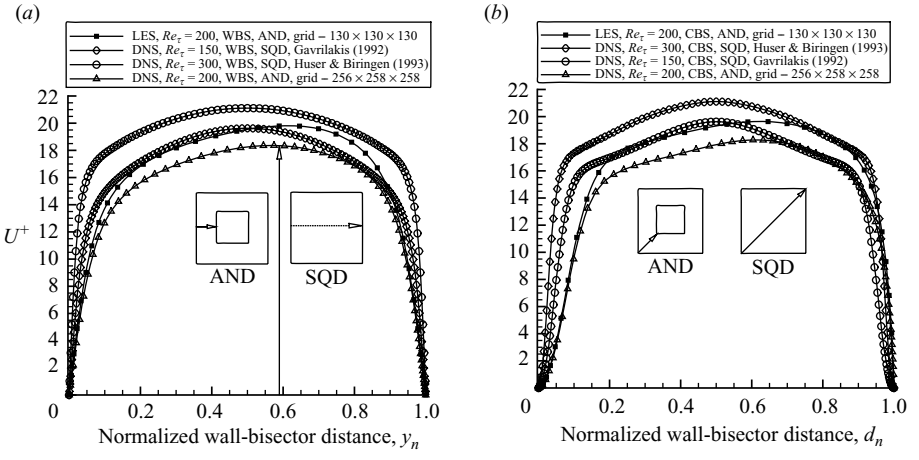

FIGURE 5. Mean streamwise velocity along the (*a*) wall bisector (Region I) and (*b*) corner bisector (Region II and III).

Another important observation in figure 5 (*a*, *b*) is that the velocity profiles exhibited high gradients near the wall and corners and flattened quickly away from these regions. This suggests that the boundary-layer concept and analysis are valid not only in the near-wall region but can also be extended to the near-corner regions and that the corner bisector is a characteristic line for the analysis. This idea was implicitly used in the LES of Xu & Pollard (2001). The analysis of the current DNS led to the derivation of the 'law-of-the-corner' formulations that provide quantitative descriptions of the TDSF effects on the bulge of the streamwise-velocity contours in the corner vicinity, supplementing the qualitative observations in Nikuradse (1930).

3.1.2. *Analysis of the streamwise velocity in the near-wall and near-corner regions*

The near-wall behaviour of the mean streamwise velocity U^+ was validated by the 'law-of-the-wall' as shown in figure 6(*a*, *b*). The comparison also included the LES and DNS at both lower and higher Reynolds numbers. In the inner region ($y^+ \leqslant 10$), the U^+ near the inner and outer walls agreed well with each other for both the

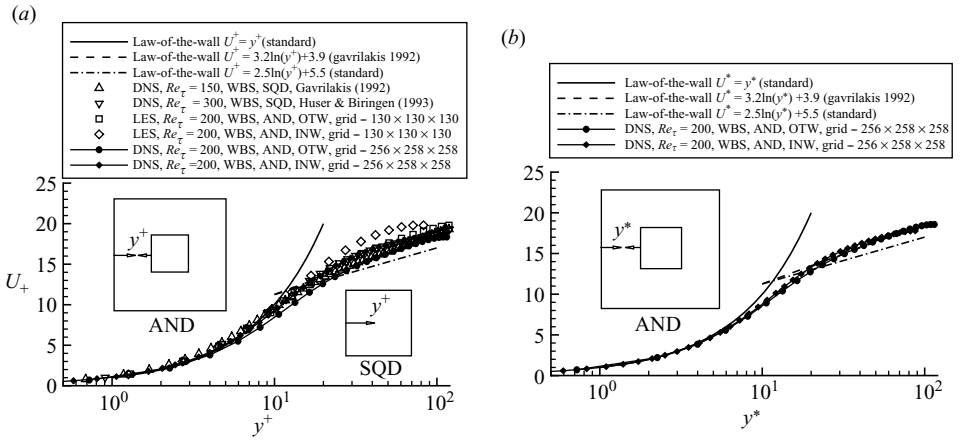

FIGURE 6. Mean streamwise velocity behaviour in the near-wall region (Region I) (*a*) scaled by the mean frictional velocity and (*b*) scaled by the local frictional velocity.

LES and DNS and were in good accord with the linear-diffusion relationship. In the logarithmic region ($20 \leqslant y^+ \leqslant 100$), the current DNS agreed better with the square duct DNS compared to the previous LES, particularly in the inner-wall region. The improvement confirmed the necessity of increasing the grid density and resolution in the inner-wall region. The over-prediction of U^+ near the inner wall in the previous LES was not caused by the high velocity gradient. Instead, the overshoot was the result of a grid-diffusion effect due to the insufficiency of the grid resolution and discretization. The slight discrepancies between the data near the inner and outer walls in figure 6(*a*) are attributed to the velocity-scale ambiguity issue for a wall-bounded turbulence (see Gavrilakis 1992). Evidently, the local frictional velocity u^* ought to be the velocity scale for the viscous sublayer, and Gavrilakis (1992) argued that the local scaling should be valid for some distance beyond the viscous sublayer. Based on this argument, U^+ was rescaled by the local value. The mean wall shear stress analysis (see § 3.1.3) gives the shear stress ratios ($\tau_w/\bar{\tau}_w$) along the wall bisector at 1.0663 for the inner wall and 0.9766 for the outer wall. The rescaled U^+, using the relationship $u^*/u_\tau = \sqrt{\tau_w/\bar{\tau}_w}$, is presented in figure 6(*b*). The two curves for the inner and outer walls overlapped almost perfectly after the rescaling and exhibited a better agreement with the 'law-of-the-wall'. This suggests that the local frictional velocity should, indeed, be used as the velocity scale. The current DNS followed the relationship $U^+ = 3.2\ln(y^+) + 3.9$ in $10 \leqslant y^+ \leqslant 100$, which is different from the conventional 'law-of-the-wall' for a flat-plate, i.e. $U^+ = 2.5\ln(y^+) + 5$. From Gavrilakis (1992), the discrepancy can be attributed to the low Reynolds number effect and the influence of the secondary flow (see the secondary flow velocity magnitude along the wall bisector in figure 9), which causes a distortion of streamwise velocity contours along the wall bisector in figure 3. However, the rescaling correction is valid only for the region in which the flow is essentially parallel to the wall and the local mean wall shear stress ratio is close to unity. As demonstrated in the following section, the strong TDSFs along corner bisector (see figure 9) caused a significant distortion of the streamwise velocity contours near the corners (see figure 3) and drastically altered the nature of the corner boundary layer. Therefore, an alternative way to characterize the corner turbulence must be developed to account for the 'damping' and 'enhancing' mechanisms identified for the concave and convex corners, respectively.

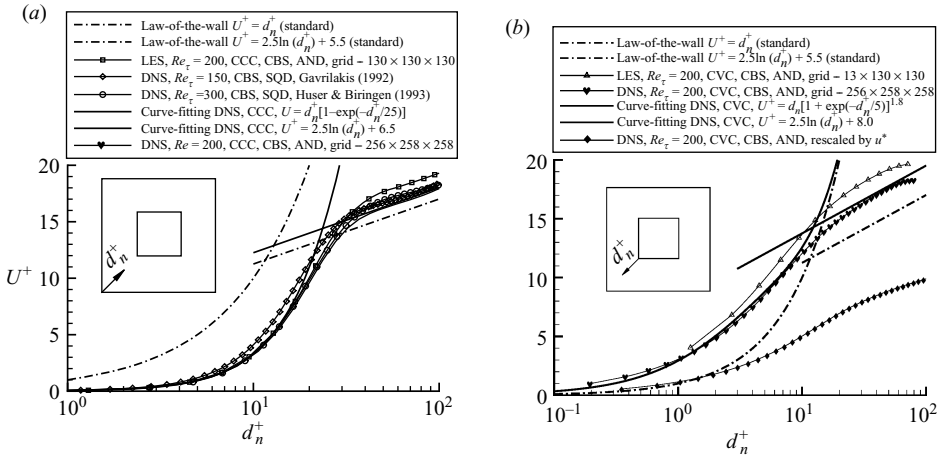

FIGURE 7. Mean streamwise velocity (a) near concave corner (Region II) and (b) near convex corner (Region III).

Following the approach proposed by von Karman (1930) for a flat-plate turbulent boundary layer, the streamwise velocity in the vicinity of the two corners along the corner bisector are plotted on the logarithmic scales in figure 7(a, b). These distributions were compared with the traditional 'law-of-the-wall', the two DNSs along the concave-corner bisector of a square duct and the existing LES for the square annular duct.

The current DNS near the concave corner presented a slight improvement compared to the previous LES, particularly in the logarithmic region, and were in a better agreement with the other two DNSs of a square duct. Therefore, the curve-fitted formulation for the concave corner remained the same as that obtained in the previous LES, i.e. in the corner boundary-layer inner region $0 \leqslant d_n^+ \leqslant 20 : U^+(d_n^+) = d_n^+(1 - e^{-d_n^+/25})$ and in the turbulent corner boundary-layer outer region $30 \leqslant d_n^+ \leqslant 100 : U^+(d_n^+) = 2.5\ln(d_n^+) + 6.5$, where d_n^+ is the normalized corner bisector distance shown in figure 5(b), equivalent to y^+ along the wall bisector. The transition point between the inner and outer layers for the concave corner occurred at $d_n^+ = 23.58$, where U^+ is equal to 14.40. A factor of $\sqrt{2}$ must be applied to convert d_n^+ to the actual length d^+in the corner bisector direction, which yields a relation of $U^+(d^+) = 2.5\ln(d^+) + 5.6$ in the concave-corner outer region. The consistency with the relation for smooth flat-plate outer layer suggests that the concave corner does not impose any roughness effect on the turbulent outer layer. Since the local mean frictional velocity u^* is zero near the concave corner (see figure 10), the mean frictional velocity u_τ becomes the only appropriate velocity scale in this region, and a damping factor $(1 - e^{-d_n^+/25})$ proves to be appropriate to account for the damping characteristics of the concave 90° corner boundary layer.

Now the attention is switched to the convex corner. Figure 7(b) shows a significant improvement in the current DNS compared to the LES in Xu & Pollard (2001). The LES grid was sparse near the convex 90° corner, and more grid points were required well into the region of $d_n^+ \leqslant 1.0$ to resolve the convex-corner boundary layer. The first grid point near the convex corner was set at $d_n^+ = 0.195$, and five grid points were placed in $d_n^+ \leqslant 1.0$. The $U^+(d_n^+)$ dependence near the convex 90° corner was curve-fitted, as $U^+ = d_n^+(1 + e^{-d_n^+/5})^{1.8}$ in the inner layer of $0 \leqslant d_n^+ \leqslant 10$.

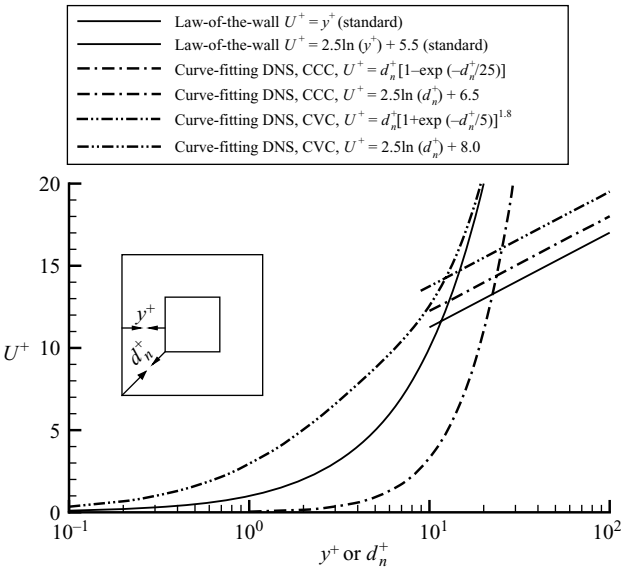

FIGURE 8. Formulations of the 'law-of-the-wall' and 'law-of-the-corner'.

The outer-layer relationship $U^+ = 2.5\ln(d_n^+) + 8.0$ was in good accord with the computation in $20 \leqslant d_n^+ \leqslant 100$. If d_n^+ is converted to the actual distance d^+, the outer-layer formulation is rewritten as $U^+ = 2.5\ln(d^+) + 7.1$. The constant (=7.1) is significantly higher than the conventional value (5.0 to 5.5) for a smooth surface. This observation concludes that the behaviour of a convex corner can be interpreted as or equivalent to a high wall-roughness effect. Near the convex corner, the two formulations yielded a transition point from the inner layer to the outer layer at $d_n^+ = 12.35$ with U^+ equal to 14.29. The transition from the inner to outer layer occurred almost at the same U^+ value (around 14.3) for both the concave and convex 90° corners; however, the distance away from the corner tip was doubled from $d_n^+ = 12.35$ for the convex 90° corner to $d_n^+ = 23.58$ for the concave 90° corner, whereas the transition point for flat plate is well known at $y^+ = U^+ = 11.6$. Although the local mean frictional velocity u^* is not zero for a convex corner, the extremely thin boundary layer shown in figure 7(*b*) suggests that u^*, as a velocity scale, is valid only within a very small d_n^* range. The curve normalized by u^* agrees with the viscous inner layer relation $U^* = d_n^*$ only within a small distance of $d_n^* \leqslant 2.0$. Therefore, an alternative way to characterize the convex-corner boundary layer must be developed to account for the enhancing mechanism, as opposed to the damping mechanism for a concave 90° corner. Figure 7(*b*) proves that the enhancing factor $(1 + e^{-d_n^+/5})^{1.8}$ produces a fairly accurate velocity profile within a distance of $0 \leqslant d_n^+ \leqslant 10$.

Due to the prominent TDSF, the nature of the corner boundary layer significantly differs from that of the flat-plate boundary layer. Towards this end, two distinctive mechanisms, namely damping and enhancing effects, are identified for the concave and convex corner turbulence, respectively. The concave and convex 90° corners impose a damping factor of $1 - e^{-d_n^+/25}$ and an enhancing factor of $(1 + e^{-d_n^+/5})^{1.8}$, respectively, onto the turbulent sublayer diffusion in the near-corner regions. Figure 8 highlights the curves of the 'law-of-the-wall' and 'law-of-the-corner' in one graph. The 'law-of-the-wall' is, in fact, a neutral curve that represents the situation with very small (or ideally zero) secondary flow. Figure 9 compares the secondary velocity

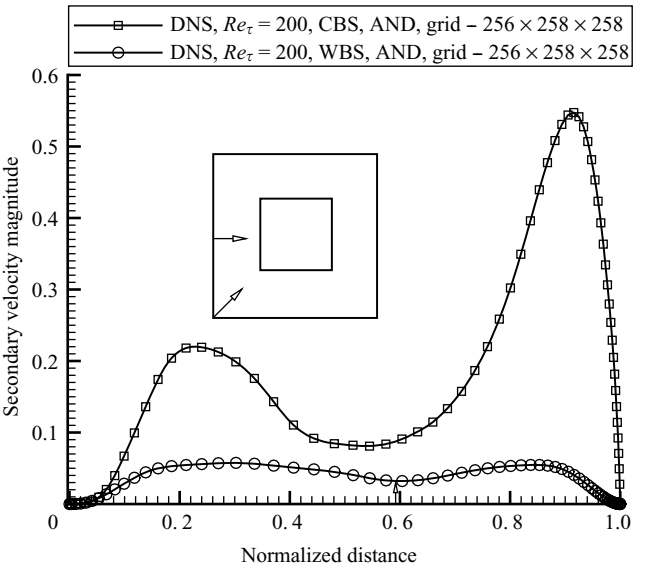

FIGURE 9. Comparison of the mean secondary flow velocity along the corner bisector and wall bisector.

magnitudes along the corner and wall bisectors. The TDSF along the corner bisector is at least a half order of magnitude larger than that along the wall bisector. When the turbulence is subjected to a TDSF pointing towards the corner (concave corner), the neutral velocity profile is pushed downward (see figure 7*a*) by the TDSF. Therefore a damping factor should apply to adjust the neutral curve to the one affected by the TDSF. For turbulence with a TDSF pointing away from the corner (convex corner), the neutral velocity profile is lifted upward (see figure 7*b*) by the TDSF, and an enhancing factor is required to correct the neutral curve to the one enhanced by the TDSF. The damping function first presented in van Driest (1956) was in a general form of $1-e^{-y/A}$, with A being the characteristic length at which an eddy is effectively dampened. In contrast to a damping effect, an enhancing function is developed here in a general form of $1+e^{-y/A}$, where A is the characteristic length within which the enhancement is effective. Curve fitting the DNS near the concave 90° corner gave an optimal value of $A = 25$, coinciding with the value proposed by van Driest (1956) for the flat-plate damping effect. However, the curve fitting near the convex 90° corner yielded an optimal value of $A = 5$, which is justified by the much thinner boundary layer near the convex 90° corner.

A question that naturally arises is what determines the power of the enhancing factor (=1.8), and what is its physical implication? The answer is inspired by the statement in Gavrilakis (1992): "[O]f the three velocity scales available, namely U_0, U_b and u_τ, the frictional velocity is usually deemed the most suitable choice for bounded turbulent flows since its value can be directly related to the turbulent stress field. The variation of the local mean wall stress, and therefore the local friction velocity, over the duct boundaries introduces an ambiguity as to which scale should be used. Within the viscous sublayer the local value is the correct choice." Since the velocity scale in the formulation near the convex corner, $U^+ = d_n^+(1+e^{-d_n^+/5})^{1.8}$, is based on the mean frictional velocity u_τ, the power of the enhancement factor should carry the information of the local friction velocity and must be a non-dimensional parameter. Therefore,

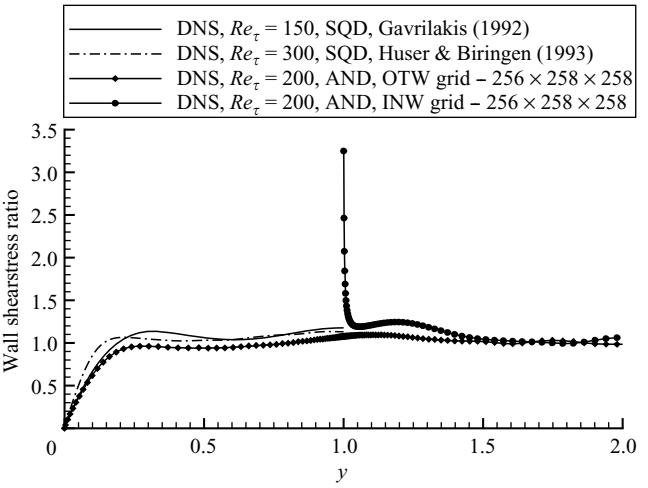

FIGURE 10. Wall shear stress ratio along the inner and outer walls of the square annular duct.

a rational guess is that the power is the ratio of the local and the mean friction velocities, u^*/u_τ. The following analysis of the wall shear stress ratio provides a strong verification of this conjecture, leading to a more general form of the velocity profile near a convex corner, $U^+ = d_n^+ \left(1 + e^{-d_n^+/A}\right)^{u^*/u_\tau}$. The universality of the formulation must be subject to further validation for more convex-corner flow configurations.

3.1.3. *Analysis of the wall shear stress*

The ensemble-averaged wall shear stress ratio, calculated by $\tau_w/\bar{\tau}_w = \left(\partial U^+/\partial y^+\right)_w$, is plotted in figure 10 as a function of the distance along the side walls of both the square and annular ducts. The $\tau_w/\bar{\tau}_w$ in the concave-corner region ($y \leqslant 0.25$) of the annular duct is similar and comparable to those of a square duct due to the fact that the flow behaviour is essentially dominated by the concave 90° corner. The shear stress ratio at the concave corner tip was zero and gradually increased to unity over the region of $0 \leqslant y \leqslant 0.25$. By taking the derivative of velocity near the concave corner, $U^+(d_n^+) = d_n^+(1 - e^{-d_n^+/25})$, $\tau_w/\bar{\tau}_w = (\partial U^+/\partial d_n^+)_w$ approaches zero because of the effect of the van Driest damping function. The convex 90° corner caused a sharp increase in $\tau_w/\bar{\tau}_w$ within a small distance of $1.0 \leqslant y \leqslant 1.06$. The peak of $\tau_w/\bar{\tau}_w$ from the present DNS was 3.261, whereas the LES in Xu & Pollard (2001) significantly under-predicted this peak (= 1.62) due to the poor grid resolution. By taking the derivative of velocity near the convex corner, $U^+ = d_n^+(1 + e^{-d_n^+/5})^{1.8}$, $\tau_w/\bar{\tau}_w = (\partial U^+/\partial d_n^+)_w$ at $d_n^+ = 0$ is equal to 3.48. The major contribution is from the enhancing factor $(1 + e^{-d_n^+/5})^{1.8}$. Therefore, the three types of turbulent boundary layers can be identified from their distinct characteristics in terms of the shear stress ratio. A flat-plate boundary layer is characterized by a shear stress ratio near unity due to the inner-wall relationship $U^+(y^+) = y^+$. A concave 90° corner boundary layer has a zero shear stress ratio due to the damping effect of $(1 - e^{-d_n^+/25})$. A convex 90° corner boundary layer has a shear stress ratio of 3.261 based on the current grid resolution, which yields a local friction velocity ratio of $u^*/u_\tau = \sqrt{\tau_w/\bar{\tau}_w} = 1.806$. The value coincides with the power of the enhancing factor, which confirms the conjecture in § 3.1.2 and leads to a

Benchmark	$z_1 = 0.1000$	$z_1 = 0.1600$	$z_1 = 0.3000$	$z_1 = 0.5000$	$z_1 = 0.7000$
Present DNS	$z_2 = 0.0815$	$z_2 = 0.1304$	$z_2 = 0.2445$	$z_2 = 0.4075$	$z_2 = 0.5705$

TABLE 2. z stations at which the current DNS results and benchmark data were compared.

more general and universal formulation for the velocity profile near a convex corner, $U^+ = d_n^+(1 + e^{-d_n^+/A})^{u^*/u_\tau}$.

3.1.4. *Flow similarity rule in concave and convex 90° corner regions*

The DNS of Gavrilakis (1992) and the experiment from Cheesewright *et al.* (1990) were used to quantitatively validate the current DNS. As shown in figure 4(*a*), the TDSF pattern was similar for both the square and annular ducts near the concave corner, which suggests that the flow features, including both the streamwise velocity and TDSF, ought to be at least qualitatively comparable. The flow similarity near a corner is aimed at establishing a rule for a quantitative comparison. The key step is to identify the trimming parameters that make the flow near a corner universally comparable. Since the argument is based on the similarity of the TDSF near a concave 90° corner, the locations of the mean TDSF vortex core ought to be the key parameters for trimming the flows near the concave corners. The vortex core from Gavrilakis (1992) was located at $(y_1, z_1) = (0.206, 0.500)$, whereas the current DNS gave the vortex core at $(y_2, z_2) = (0.164, 0.407)$. Therefore, the trimming parameters are defined as $y_2/y_1 = 0.797$ in the y direction and $z_2/z_1 = 0.815$ in the z direction. Table 2 provides the z stations at which the measurements from Cheesewright *et al.* (1990) and the DNS from Gavrilakis (1992) were taken and the corresponding z stations ($z_2 = z_1 \times 0.815$) at which the present DNS data were extracted for comparison.

Figure 11(*a*, *b*) presents the streamwise velocity (U/U_0) and TDSF component in the z direction (W/U_0), respectively, at four z stations near the concave corner, including the data before and after the correction. After corrected by the trimming parameters defined based on the location of the vortex core ($y_2 = y_1 \times 0.797$), the present DNSs were compared with the data from Cheesewright *et al.* (1990) and Gavrilakis (1992). The corrected data, roughly in the region $(y, z) = (0–0.5, 0–0.5)$, were found in much better quantitative agreement with the benchmarks than the uncorrected data, which manifests a strong support for the existence of the flow similarity and the correctness of the trimming parameters selection. Outside the concave corner region, i.e. $(y, z) = (\geqslant 0.6, \geqslant 0.6)$, the flow field was affected by the existence of the inner side walls and the convex corner. Therefore, some deviations were apparent. This analysis indicated that the turbulence was strongly flow-configuration dependent, and the flow features were very local. For example the flow features for a concave 90° corner flow were similar, regardless of whether the domain was a square annular duct or a square duct, provided the mean flow near the corner was symmetric. Therefore, it is reasonable to believe that the 'law-of-the-corner' shown in figure 8 possesses some degree of universality under the symmetric mean flow conditions. Based on the same argument, the flow around a convex corner also possesses a similarity property. Again, the vortex core location near the convex corner ought to be the key parameter for trimming the flows for comparison. The location of the vortex core near the convex corner was $(y, z) = (0.781, 1.069)$, and the region of dominance for the convex corner vortex was roughly within the range of $(y, z) = (0.7–1.3, 0.7–1.3)$. The information is provided

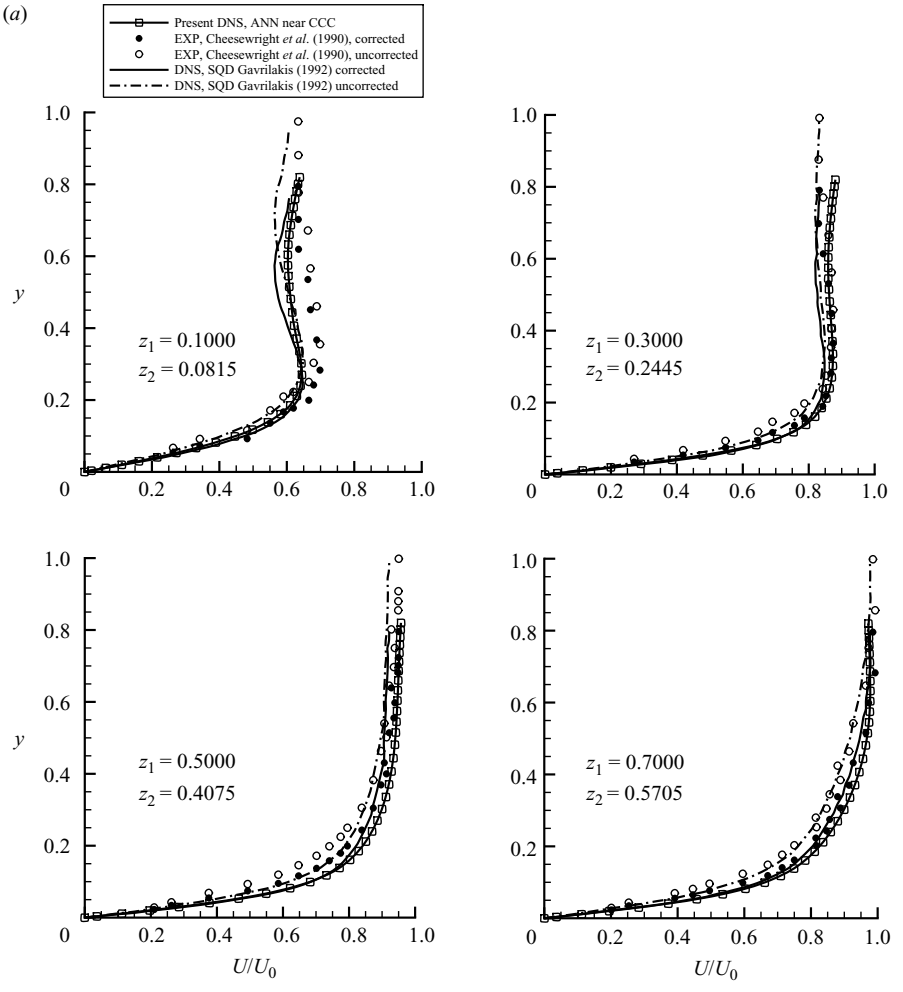

FIGURE 11. For caption see next page.

for future comparison and validation with other convex-corner flow configurations, such as the TDSF structures near a riblet peak reported by Choi *et al.* (1993).

3.2. *Turbulence statistics*

3.2.1. *Turbulence energy spectra (TES)*

Two groups of sampling points, shown in figure 2, were selected to study the TES at different scales of motion: Group I along the wall bisector and Group II along the corner bisector. Since the streamwise grid number was 256, a minimum number of four grid points were needed to represent one sinusoidal cycle. The limiting cutoff wave number is roughly estimated to be between 60 and 70, and the signals beyond this range can be considered as noise. Figure 12(a, b) presents the TES at these sampling points. These spectra were qualitatively checked by the Kolmogorov $-5/3$ law (see Kolmogorov 1962), which characteristically divided the entire spectrum into regimes: the large scales, the inertial range and the small or Kolmogorov scales. The spectra at the limiting cutoff wave numbers had larger negative slopes than the $-5/3$ law, which indicates that the grid resolution in the x direction was sufficient to

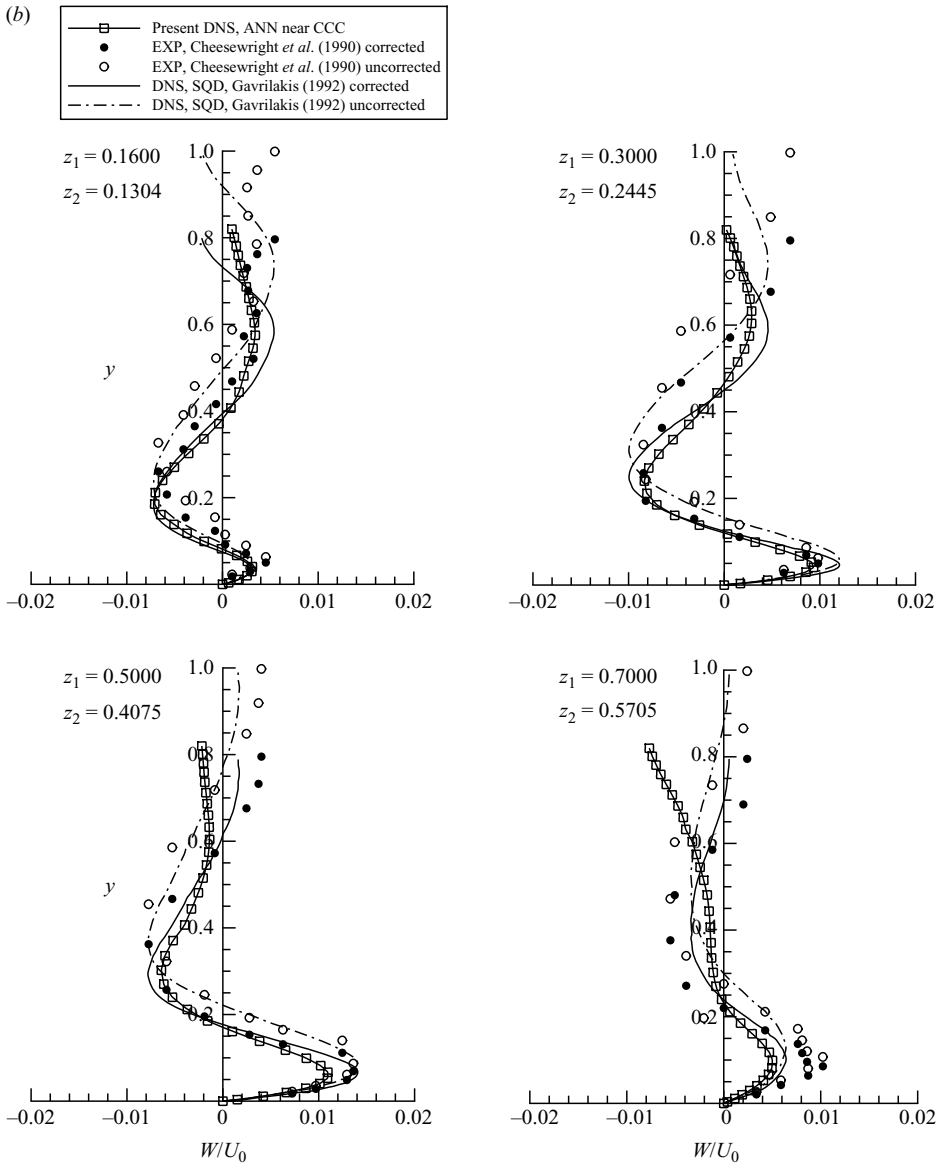

FIGURE 11. Comparisons of the (*a*) streamwise velocity profiles and (*b*) mean secondary velocity near the concave corner in the z direction.

resolve the turbulence motions down to Kolmogorov scales. However, the conclusion must be made with a caution that the larger negative slope might be due to the under-resolution of the current grid for those high wavenumber motions, and a grid refinement study is warranted in the streamwise direction to resolve the issue.

The major fundamental postulation in the constitutive equation for a Newtonian fluid is the isotropy assumption (see Wang 1982 and Warsi 1993), which warrants the stress–strain coefficient tensor $\boldsymbol{E}_{ijkm}$ reducing to two independent scalar invariants (μ, λ) known as the first (molecular) and second (volume) coefficients of viscosity. To study turbulence motions and their effects on the mean flow, Kolmogorov

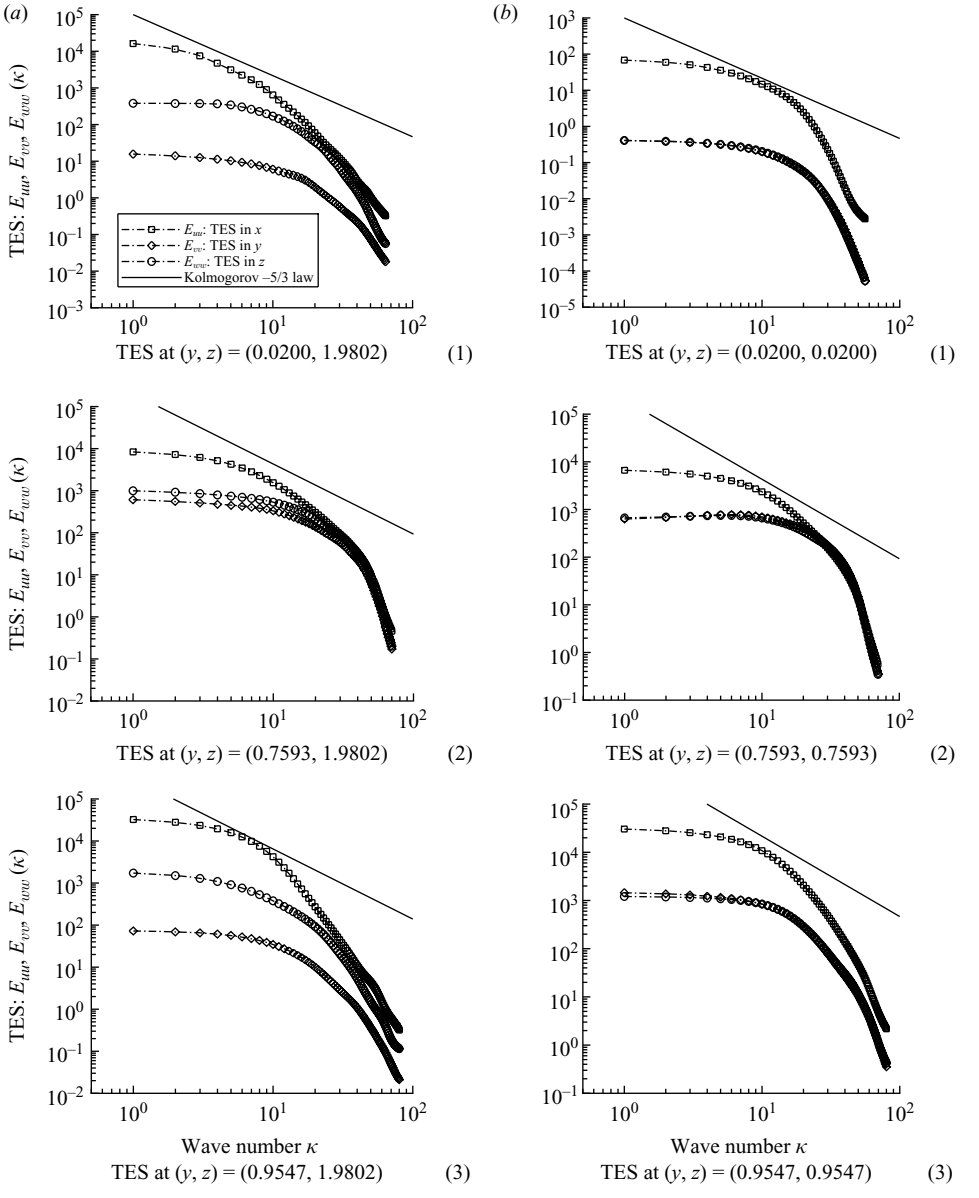

FIGURE 12. (*a*) TES along the wall bisector. (*b*) TES along the corner bisector.

(1942) proposed a generalized form of Boussinesq's hypothesis, $\rho\overline{u_i' u_j'} = A\delta_{ij} + \mu_T(\partial\bar{u}_i/\partial x_j + \partial\bar{u}_j/\partial x_i)$, based on an analogy of the motions between fluid particles and turbulence eddies, resulting in the well-known turbulent eddy viscosity μ_T. The isotropy assumption of turbulent eddy motions implicitly contained in the Boussinesq's hypothesis is disputable and the DNS data enables a direct interrogation of the issue. Analyses of the turbulence anisotropy in the square annular duct, as demonstrated by the TES in figure 12, provide better understandings of the turbulence features in different flow regimes, such as near-wall, near-corner and homogeneous

flows, and result in the re-evaluation of the validity of the conventional turbulent eddy viscosity concept.

The strong anisotropies presented in figure 12 are the dominant features in the entire flow domain for the large-scale motions with the wavenumbers ranging from 1 to 10. These anisotropies are highly flow-geometry dependent. Therefore, the conventional eddy viscosity concept loses its validity for the motion at these scales, which is well known to cause the failure of RANS methods. As demonstrated in the second parts of figure 12(a, b), the homogeneous turbulence away from the wall and corner regions is characterized by strong anisotropy and flow-configuration dependence in large-scale motions. As the energy cascades down to small-scale motions, these energy spectra approach an isotropic state in three spatial directions. This observation suggests the validity of applying the turbulent eddy viscosity assumption in these regions to represent the turbulence motions at sufficiently small scales. The current results indicate that these small scales are roughly the motions beyond a wavenumber of 30, and wavenumbers between 10 and 30 correspond to the transition (or inertia) regime characterized by the $-5/3$ slope. These characteristics of turbulence are consistent with the philosophy of LES. However, in the near-wall and near-corner regions, the anisotropy of the turbulence motions persists, even at small scales, shown in the first and third parts of figure 12(a, b). Again, the anisotropy is strongly flow-configuration and flow-region dependent. For instance the flow is always isotropic in the y and z directions along the corner bisector because of the symmetric geometry but very anisotropic compared in the streamwise direction, as shown in figure 12(b). This observation implies that the conventional (scalar) eddy viscosity μ_T is not sufficient to represent the anisotropic turbulence motions at small scales in some specific regions, such as the vicinities of walls and corners. Therefore, more accurate RANS closure model or LES subgrid scale models are recommended to be developed in future by considering the turbulence eddy viscosity as a tensor μ_{Tijkm} rather than a scalar in Boussinesq's hypothesis, i.e. $\rho\overline{u_i'u_j'} = A\delta_{ij} + \mu_{Tijkm}(\partial\bar{u}_k/\partial x_m + \partial\bar{u}_m/\partial x_k)$, where the indices i, j, k, m take the values of 1, 2, 3, that represent three spatial dimensions, and the repeated indices k, m imply the Einstein summation. DNS database should be utilized to derive appropriate simplifications for the eddy viscosity tensor and to calibrate each tensor component in μ_{Tijkm} so that the anisotropy issue can be sufficiently addressed.

3.2.2. *Turbulence Reynolds stresses*

The Reynolds stresses, $\overline{u'u'}$, $\overline{u'v'}$, $\overline{v'v'}$ and $\overline{v'w'}$, were accumulated and averaged over a period of LETOTs = 9 (from 2 to 10 LETOT). Figure 13 shows the distributions over the lower-left quadrant of the square annular duct, using contour plots. The Reynolds stress distributions for the other quadrants can easily be obtained through a symmetrical mirroring or reflecting transformation with respect to the corresponding axes or origin. The four stress components in figure 13 clearly indicate that the Reynolds stress distributions are highly non-uniform and strongly flow geometry dependent, particularly near the regions of walls, concave and convex corners.

Figure 14(a–b) presents the streamwise and cross-streamwise turbulence intensities, $u'_{r.m.s.}$, $v'_{r.m.s.}$ and $w'_{r.m.s.}$, scaled by u_τ, along the lines of $z = 1.00$ and 1.98. These data were compared with previous LES from Xu & Pollard (2001) and the DNS from Gavrilakis (1992) and Huser & Biringen (1993). A tangible amount of grid dependence was found for the streamwise turbulence intensities. Compared with the current DNS, the previous LES generally over-predicted the turbulence intensities of $u'_{r.m.s.}$, which is consistent with the observation from Huser & Biringen (1993),

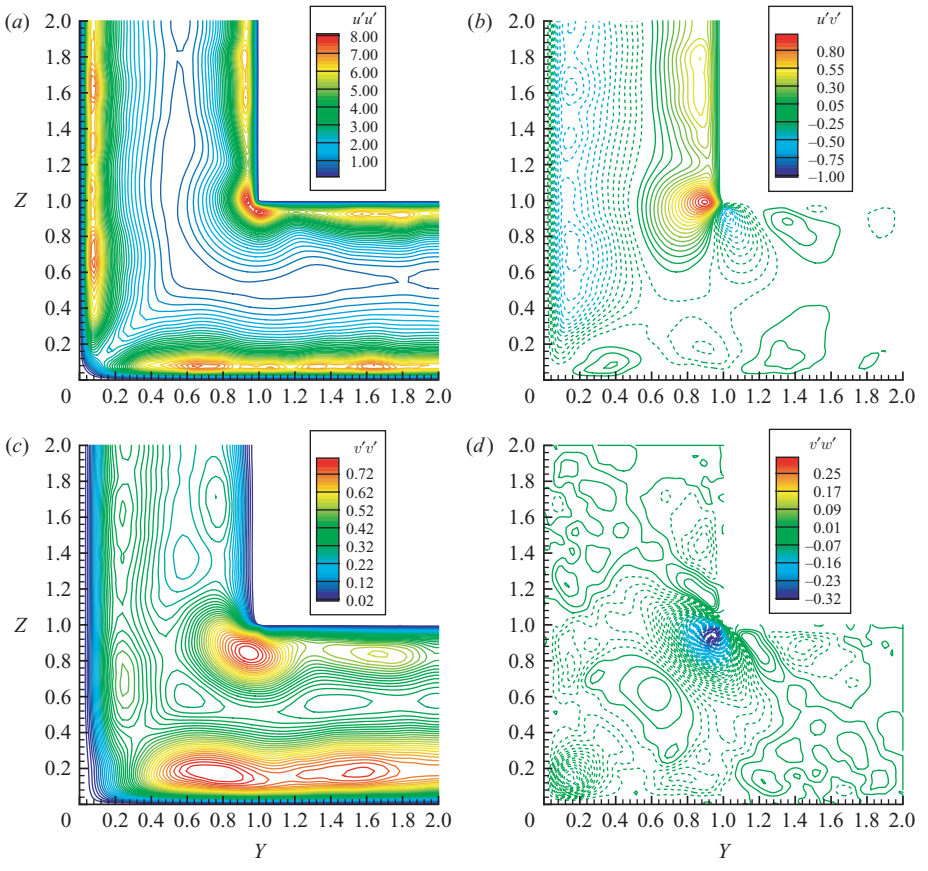

FIGURE 13. Reynolds stress distributions scaled by u_τ: (*a*) $\overline{u'u'}$; (*b*) $\overline{u'v'}$; (c) $\overline{v'v'}$; (*d*) $\overline{v'w'}$.

'[I]n the present results, the $u'_{r.m.s.}$ decrease with increasing grid resolution', and the comment made by Rai & Moin (1991), '[T]he upwind-biased scheme has a tendency to overpredict the maximum value in $u'_{r.m.s.}$ when the computation is under-resolved'. The current DNS predictions were closer to the DNS from Gavrilakis (1992) in terms of both the peak and valley values of the $u'_{r.m.s.}$ along $z = 1.00$ and 1.98. The distributions of both the $v'_{r.m.s.}$ and $w'_{r.m.s.}$ were by no means close to symmetry along the wall bisector. This observation indicates that the TDSF induced by the convex corner imposed a non-negligible effect on the flow near the wall bisector and made the flow pattern deviate from a conventional channel flow.

Most existing experiments, such as those by Kreplin & Eckelmann (1979), Niederschulte (1989) and Nishino & Kasagi (1989), were obtained for turbulent flows in plane channel configurations. The Reynolds stresses from these flows are compared to the current DNS along the two lines illustrated in figure 14(*b*), corresponding to $z = 1.00$ (along a line parallel to the bottom of the duct and extending from the convex corner) and 1.98 (along wall bisector). DNS data along the wall bisector of a square duct from Gavrilakis (1992) and Huser & Biringen (1993) are also included. Although the flow in the square annular duct is asymmetric along the wall bisector, as shown in figures 13 and 14, it can still be argued that the Reynolds stress patterns are not that far away from those of a channel flow due to the effects of the inner and

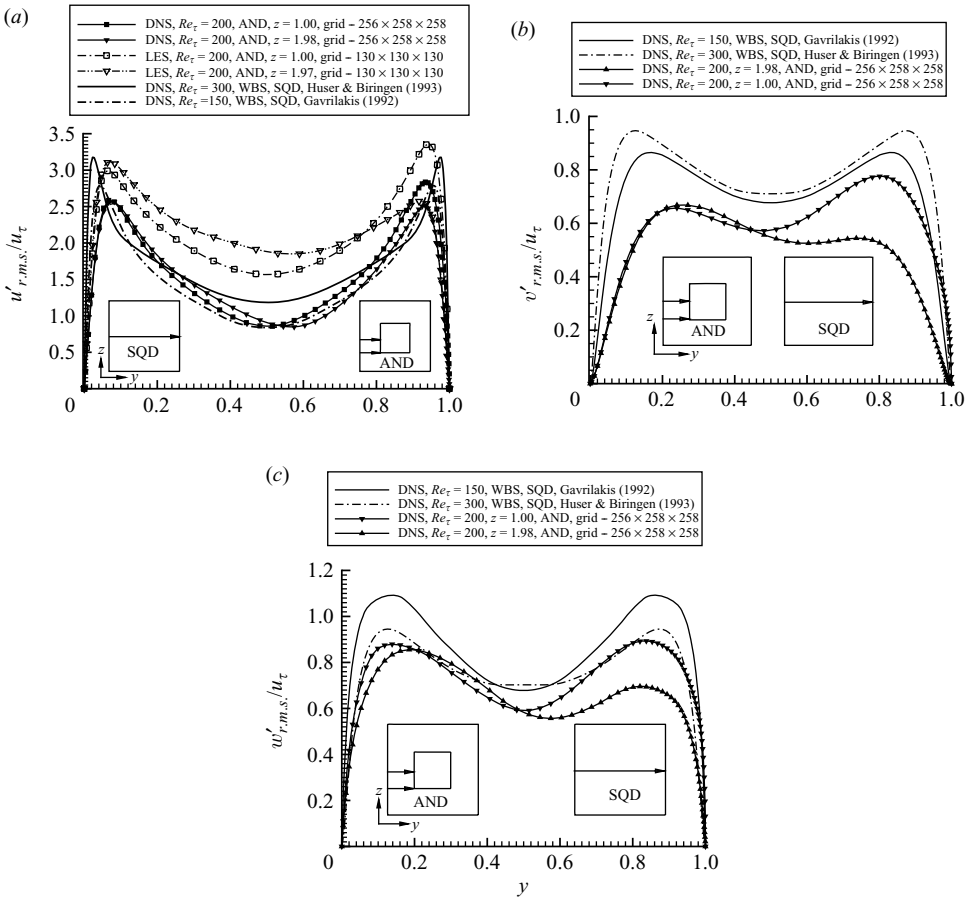

FIGURE 14. Streamwise and cross-streamwise turbulence intensities (*a*) $u'_{r.m.s.}$, (*b*) $v'_{r.m.s.}$ and (*c*) $w'_{r.m.s.}$ scaled by u_τ along $z = 1.98$ (wall bisector) and $z = 1.00$.

outer side walls and the symmetry requirement perpendicular to the wall bisector. However, for the line at $z = 1.00$ extending from the convex corner, the flow near the outer wall is expected to be close to channel flow, while some deviations are anticipated near the convex corner. These comparisons present a qualitative check, rather than a point-to-point validation, of the flow behaviour, particularly near the wall and the corner. Since the experiments were all scaled by the local mean frictional velocity, and the current DNSs were rescaled by u^* near the convex corner, the results scaled by u_τ are also included for comparison purpose. The concave-corner region is considered, where the current DNSs, after being corrected by the trimming parameters (secondary vortex core location) given in § 3.1.4, are compared with the DNS from Gavrilakis (1992) and the experiment from Cheesewright *et al.* (1990). The experiment and Gavrilakis's DNS are inclusively referred to as the benchmark data.

Plotted in figure 15(*a–c*) are the turbulence intensities of $u'_{r.m.s.}$, $v'_{r.m.s.}$ and $w'_{r.m.s.}$ scaled by u^* along $z = 1.00$ and 1.98. These data are compared to the DNSs from Gavrilakis (1992) and Huser & Biringen (1993) along the wall bisector of a square duct. The $u'_{r.m.s.}$ variations shown in figure 15(*a*) were comparable to the benchmark data in terms of their peak and valley values near the outer wall. The gradients of the $u'_{r.m.s.}$ curves were somewhat different, which is attributed to the Reynolds

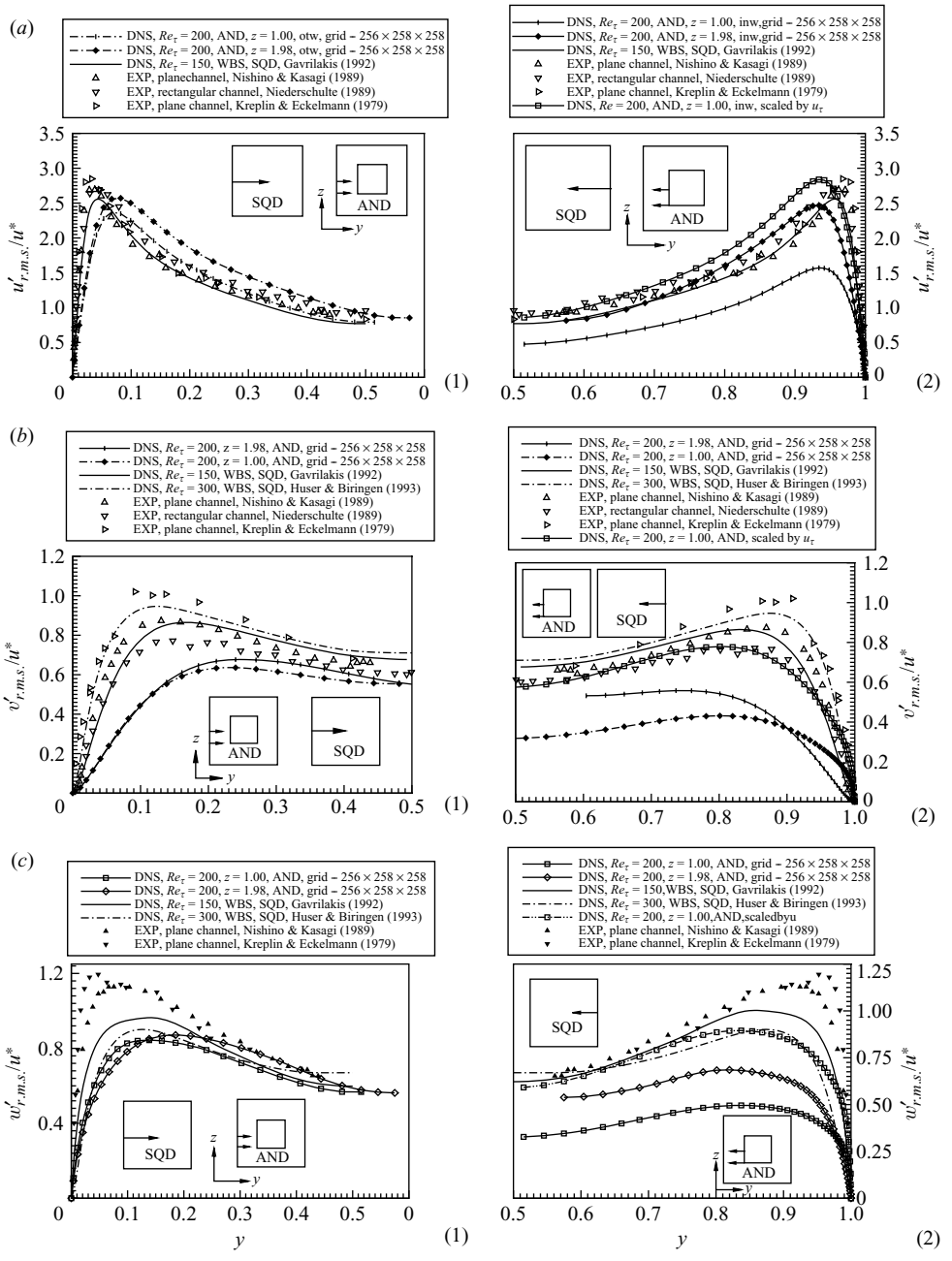

FIGURE 15. (*a*) Streamwise turbulence intensity $u'_{r.m.s.}$ scaled by u^* (1) near the outer walls along $z = 1.00$ and 1.98 and (2) near the inner wall along $z = 1.00$ and 1.98. (*b*) Cross-streamwise turbulence intensity $v'_{r.m.s.}$ scaled by u^* (1) near the outer walls along $z = 1.00$ and 1.98 and (2) near the inner wall along $z = 1.00$ and 1.98. (*c*) Cross-streamwise turbulence intensity $w'_{r.m.s.}$ scaled by u^* (1) near the outer walls along $z = 1.00$ and 1.98 and (2) near the inner wall along $z = 1.00$ and 1.98.

number difference and the TDSF effects. Near the inner wall, the DNS predictions along the wall bisector were close to the benchmark data, but significant discrepancies were found near the convex corner due to the extremely high u^*. The curve scaled by u_τ was in good accord with the benchmark data. Since the ratio of the local to mean wall shear stresses ($\tau_w/\bar{\tau}_w$) is close to unity along the wall bisector for the channel and square duct flows, the benchmark data are expected not to change very much if rescaled using u_τ. Therefore, the mean frictional velocity u_τ is more appropriately applied as the velocity scale near the convex corner. For the cross-streamwise turbulence intensities, i.e. $v'_{r.m.s.}$ and $w'_{r.m.s.}$, the distribution patterns along $z = 1.00$ and 1.98 were similar to the benchmark data near the outer wall (see the first parts of figure 15b, c); however, the gradients near the outer wall were lower than the benchmark data. Near the inner wall (see the second parts of figure 15b, c), both $v'_{r.m.s.}$ and $w'_{r.m.s.}$ exhibited high gradients near the convex corner ($z = 1.00$) and quite low near-wall gradients along $z = 1.98$, particularly $v'_{r.m.s.}$. The magnitudes of both $v'_{r.m.s.}$ and $w'_{r.m.s.}$ were in better agreement with the benchmark data near the convex corner if scaled by u_τ but significantly lower than the benchmark data if scaled using u^*. This observation again suggests that the mean frictional velocity u_τ ought to be used as the velocity scale near the convex corner.

The turbulence shear stress $\overline{u'v'}$ along $z = 1.00$ and 1.98, scaled by u_τ, are compared in figure 16(a) to the square duct DNS along the wall bisector. The distributions near the outer wall were quite similar to each other along $z = 1.00$ and 1.98; however, significant differences were found near the inner wall in terms of both gradients and peak magnitudes. Figure 16(b) shows $-\overline{u'v'}$ scaled by u^* along $z = 1.00$ and 1.98 near the inner and outer walls, respectively. These data were also compared to the benchmark data. The distribution patterns near the outer wall, shown in the first part of figure 16(b), were quite similar to the benchmark data, which is highlighted by a sharp increase to a peak near wall followed by a linear decrease. These patterns can be well explained by the mean streamwise momentum equation:

$$\underbrace{-\frac{\partial UV}{\partial y}-\frac{\partial UW}{\partial z}}_{\textit{convection}}\underbrace{-\frac{\partial \overline{u'v'}}{\partial y}-\frac{\partial \overline{u'w'}}{\partial y}}_{\textit{Reynolds shear stresses}}+\underbrace{\frac{\partial}{\partial y}\left(\nu\frac{\partial \bar{U}}{\partial y}\right)+\frac{\partial}{\partial z}\left(\nu\frac{\partial \bar{U}}{\partial z}\right)}_{\textit{molecular diffusion}}=\frac{\partial \bar{P}}{\partial x}. \tag{3.1}$$

The sharp gradients and the $-\overline{u'v'}$ peak near the walls are generated due to the viscous and convective effects as well as the streamwise pressure gradient, and the viscous and convective terms play important roles within this region. Outside the near-wall region, the flow is essentially dominated by the balance between the gradient of $-\overline{u'v'}$ and the streamwise pressure gradient, causing the linear decrease of $-\overline{u'v'}$. The shift between the linear decreases along $z = 1.00$ and 1.98 is caused by the flow asymmetry induced by the TDSF, as plotted in figures 4(a) and 5(a). The zero mean streamwise velocity and secondary velocity gradients occur at $y = 0.58$, as shown in figures 5(a) and 9, instead of at $y = 0.5$ for the symmetric square duct or channel flows. Therefore, the zero $-\overline{u'v'}$ point was shifted to $y = 0.58$ along the wall bisector. For the inner-wall regions, the $-\overline{u'v'}$ along $z = 1.98$ were lower than the benchmark data. The $-\overline{u'v'}$ along $z = 1.00$ line were lower than the benchmark data if scaled by u^* but higher than the benchmark data if scaled using u_τ. The $-\overline{u'v'}$ along $z = 1.00$ and 1.98 agree with each other only within a very short distance from the wall, which confirms the conclusion regarding the scaling issue of $-\overline{u'v'}$ in Gavrilakis (1992): '[B]ut beyond it (near-wall region) the scaling based on u^* becomes progressively inappropriate'.

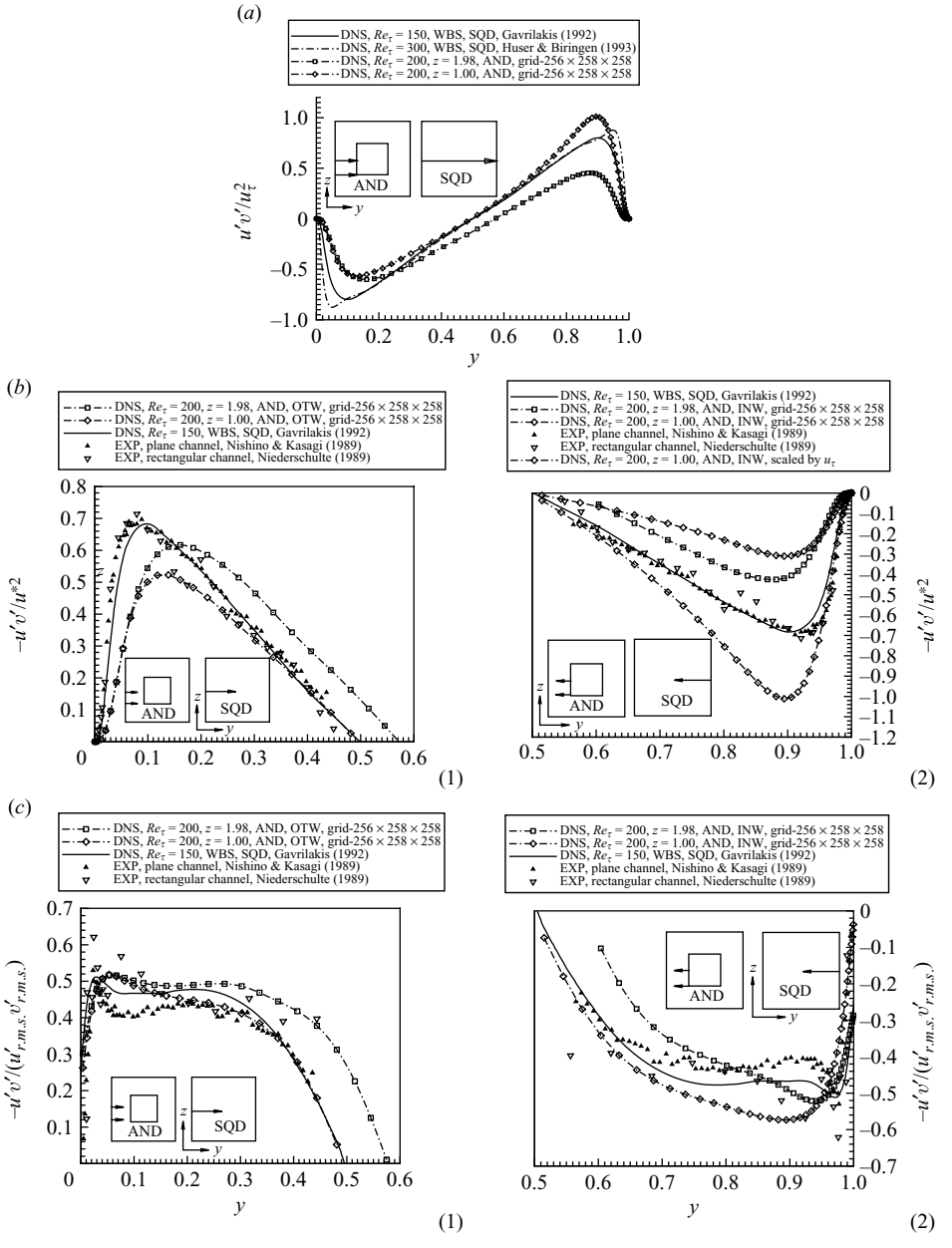

FIGURE 16. Turbulence shear stress (*a*) $\overline{u'v'}$ scaled by u_τ along $z = 1.00$ and 1.98; (*b*) $-\overline{u'v'}$ scaled by u^* (1) near the outer wall and (2) near the inner wall; (*c*) $-\overline{u'v'}$ scaled by $u'_{r.m.s.}v'_{r.m.s.}$ (1) near the outer wall and (2) near the inner wall.

Kim, Moin & Moser (1987) and Gavrilakis (1992) examined the $-\overline{u'v'}$ rescaled by the local $u'_{r.m.s.}$ and $v'_{r.m.s.}$. Figure 16(*c*) presents the $-\overline{u'v'}/(u'_{r.m.s.}v'_{r.m.s.})$ along $z = 1.00$ and 1.98 near the inner and outer walls. The near-wall maximum was evident in the current DNS, and due to the Reynolds number effect, the peaks occurred farther away from the wall compared to the benchmark data. However, the most striking observation is that the rescaling using the local $u'_{r.m.s.}$ and $v'_{r.m.s.}$ produced fairly

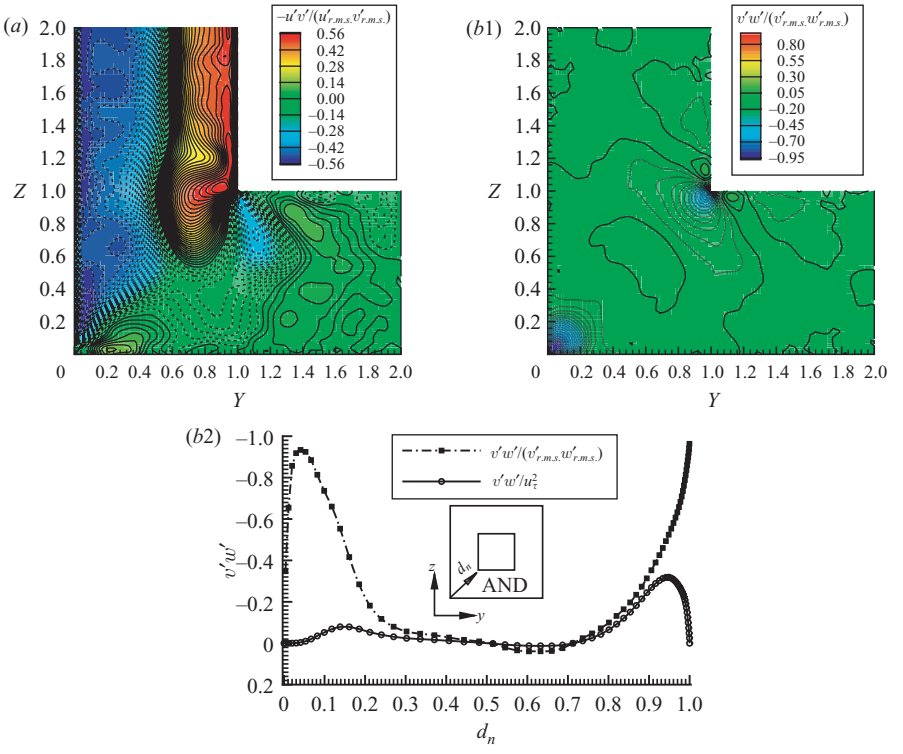

FIGURE 17. Off-diagonal Reynolds stress distributions: (*a*) $\overline{u'v'}$ scaled by $(u'_{r.m.s.}v'_{r.m.s.})$; (*b*1) $\overline{v'w'}$ scaled by $(v'_{r.m.s.}w'_{r.m.s.})$; (*b*2) $\overline{v'w'}$ along the corner bisector.

universal curves in terms of both the distribution patterns and peak values, even for the region near the convex corner. The ratio between $-\overline{u'v'}$ and local $u'_{r.m.s.}$ and $v'_{r.m.s.}$ has a fairly universal distribution patterns and characteristic peak values (around 0.5 for a flat-plate region and around 0.6 for a convex-corner region), as demonstrated in the first and second parts of figure 16(*c*). Encouraged by these findings, the off-diagonal Reynolds stress ($\overline{u'v'}$ and $\overline{v'w'}$) in the lower-left quadrant of the square annular duct were rescaled by the local values of $u'_{r.m.s.}v'_{r.m.s.}$ and $v'_{r.m.s.}w'_{r.m.s.}$, respectively, and the results are plotted in figure 17(*a*, *b*). The $\overline{u'v'}/(u'_{r.m.s.}v'_{r.m.s.})$ exhibited a more normalized distribution than the $\overline{u'v'}$ scaled by u_τ (see figure 13*b*) in the sense that the values were more universally distributed around ± 0.5 in the region encompassed by the inner and outer walls, the wall bisector and the corner bisector lines. This can be clearly seen in figure 17(*a*), where these regions are mostly covered by red and blue contours, even near the convex and concave corners. The most striking difference between the first part of figure 17(*b*) and figure 13(*d*), is that $\overline{v'w'}$ scaled by $v'_{r.m.s.}w'_{r.m.s.}$ yielded more universal distributions with peak values around unity for both the concave and convex corners. Whether this conclusion can be universally applied to other corner turbulence would be an intriguing subject to study. Since $\overline{v'w'}$, $v'_{r.m.s.}$ and $w'_{r.m.s.}$ are the key parameters for generating the TDSF (see § 3.2.3) this observation implies the contributions to TDSF from the shear stress of $\overline{v'w'}$ and the normal stresses of $v'_{r.m.s.}$ and $w'_{r.m.s.}$ are roughly equal or at least of the same order of magnitude. This issue has long been a debate as seen in Brundrett & Baines (1964), and a quantitative analysis of the issue will be provided in § 3.2.3. The corner bisector was again selected

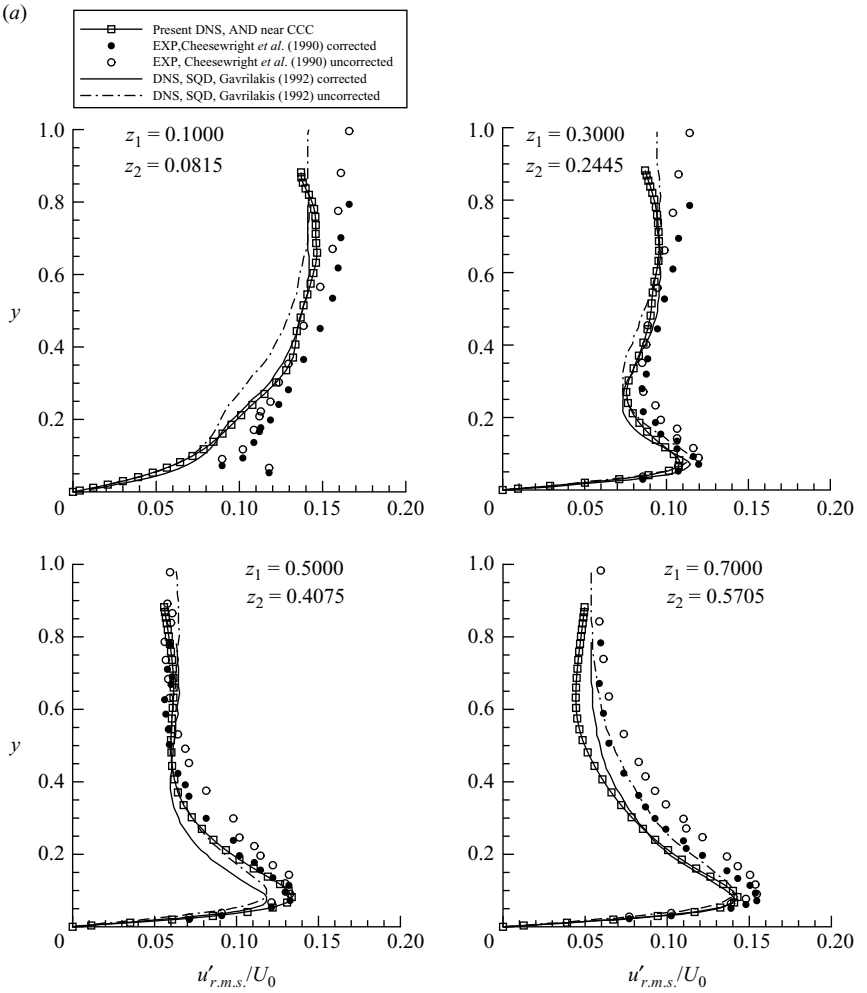

FIGURE 18. For legend see next page.

as the characteristic line to study the detailed properties of $\overline{v'w'}/(v'_{r.m.s.}w'_{r.m.s.})$ near the corners, as plotted in the second part of figure 17(*b*). Although the data presented two peaks of approximate unity near both the concave and convex corners, the manners in which $\overline{v'w'}/(v'_{r.m.s.}w'_{r.m.s.})$ approached the corners were totally different. Near the concave corner, the $\overline{v'w'}/(v'_{r.m.s.}w'_{r.m.s.})$ reached its peak at $d_n^+ = 8.2$ and then rapidly dropped to zero. However, the $\overline{v'w'}/(v'_{r.m.s.}w'_{r.m.s.})$ monotonically approached unity near the convex corner.

Now our attention is switched to the concave-corner region. Following the same trimming procedure described in § 3.1, figure 18 presents the $u'_{r.m.s.}$ and $w'_{r.m.s.}$ at the four z stations at which the measurements from Cheesewright *et al.* (1990) and the DNS from Gavrilakis (1992) were available to compare. Although some discrepancies were visible, the patterns and magnitudes of the $u'_{r.m.s.}$ and $w'_{r.m.s.}$ distributions predicted by the current DNS were similar to the benchmark data. These comparisons, together with the analyses of the mean flow field near the concave corner in § 3.1, again clearly manifest that the turbulence phenomenon is strongly flow-geometry dependent and

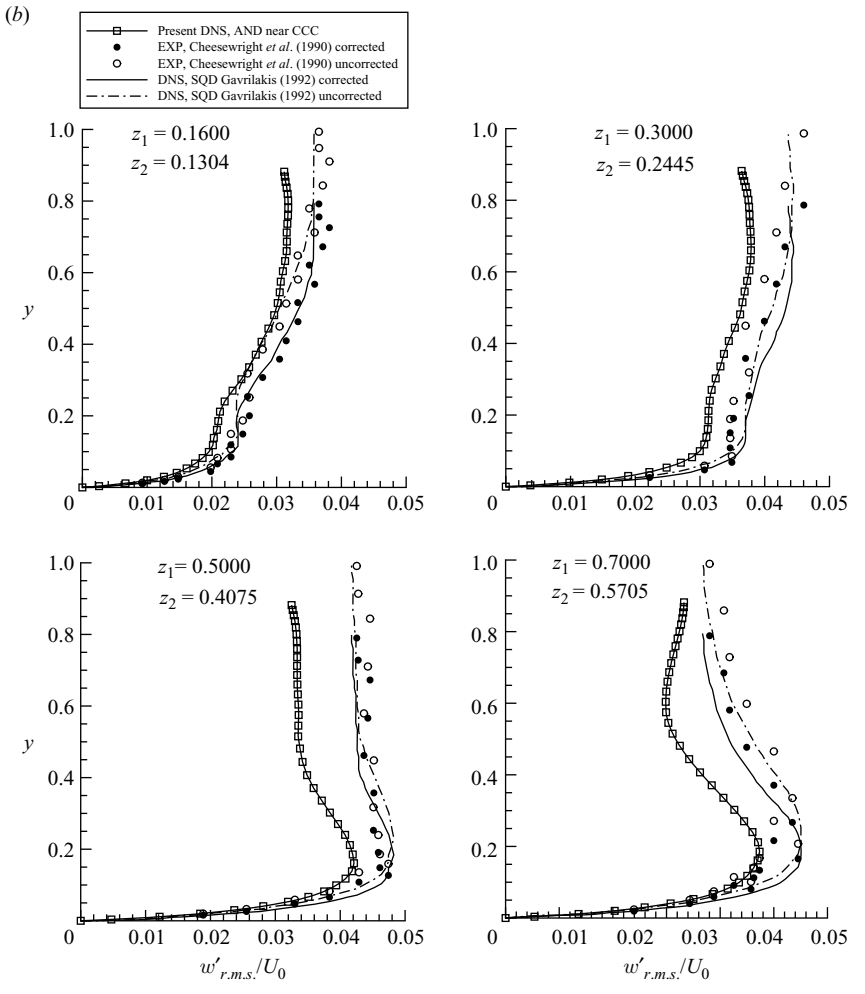

FIGURE 18. (*a*) Streamwise turbulence intensity $u'_{r.m.s.}$ and (*b*) cross-streamwise turbulence intensity $w'_{r.m.s.}$ scaled by $U_0 = 18.69$ near the concave corner.

that the features of turbulence, including both patterns and magnitudes of the mean flow field and Reynolds stresses, are locally and uniquely associated with the flow configuration. The current DNSs provide a comprehensive database to analyse the boundary layer turbulence for three configurations: a flat plate and a concave and a convex 90° corner.

The near-wall and near-corner behaviours of $u'_{r.m.s.}/U$ and $w'_{r.m.s.}/U$ were examined, since their limiting ratios approaching a wall are equal to the root mean square (r.m.s.) wall values of the spanwise vorticity (ω_z) and streamwise vorticity (ω_x). Figure 19 present the $u'_{r.m.s.}/U$ near both the outer and inner walls along $z = 1.00$ and 1.98. The measurements by Alfredsson *et al.* (1988) and Nishino & Kasagi (1989) suggested a limiting value of 0.4 for $u'_{r.m.s.}/U$ at the wall, while the square duct DNS from Gavrilakis (1992) approached 0.36. The current DNS gave values of 0.337 and 0.306 on the outer wall at $z = 1.98$ and 1.00, respectively, and 0.316 and 0.323 on the inner wall at $z = 1.98$ and 1.00, respectively. The $u'_{r.m.s.}/U$ had zero gradients in the near-wall regions at the three locations of $(y, z) = (0.00, 1.00)$, (0.00, 1.98) and (1.00,

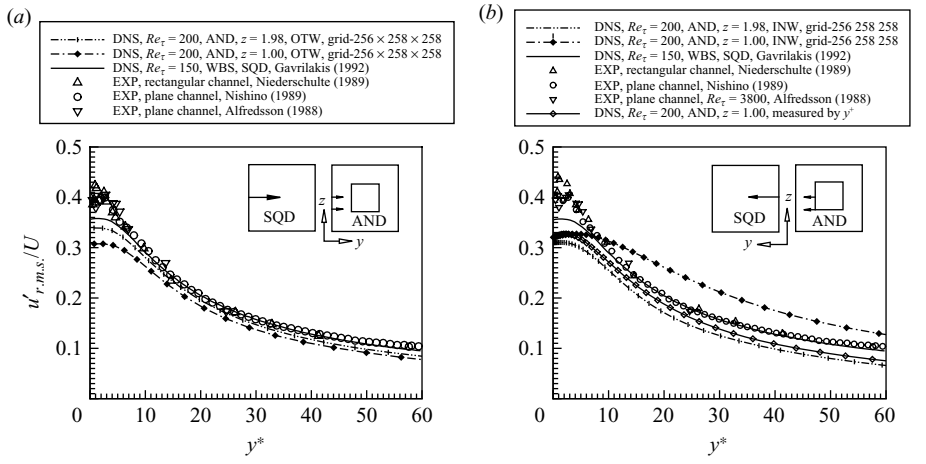

FIGURE 19. Limiting near-wall behaviour of $u'_{r.m.s.}/U$ (*a*) near the outer wall and (*b*) near the inner wall.

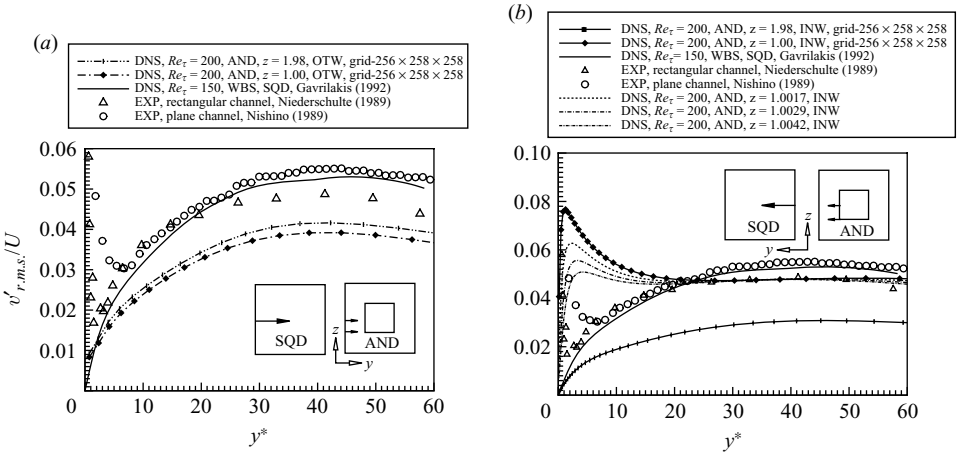

FIGURE 20. Limiting near-wall behaviour of $v'_{r.m.s.}/U$ (*a*) near the outer wall and (*b*) near the inner wall.

1.98), which is in agreement with the DNS from Gavrilakis (1992), except at the location of $(y, z) = (1.00, 1.00)$ near the inner wall and convex-corner tip at which a small negative gradient region is found in figure 19(*b*) due to the convex-corner effect. The pattern of $u'_{r.m.s.}/U$ near the inner wall and convex-corner tip was close to the $u'_{r.m.s.}/U$ profile near a flat wall when measured by y^+, but some deviations were observed when $y*$ was used as the measurement.

The limiting behaviours of $v'_{r.m.s.}/U$ at locations of $z = 1.00$ and 1.98 are plotted in figure 20 near the outer and inner walls. Along the outer wall, the current DNS presented a similar pattern compared to the DNS from Gavrilakis (1992), except that the $v'_{r.m.s.}/U$ values were lower for flow in the square annular duct. However, the experiment from both Niederschulte (1989) and Nishino & Kasagi (1989) showed a sharp increase in the near-wall region that was not captured in any DNS for the square and annular ducts. This observation suggests that the limiting values of $v'_{r.m.s.}/U$ in the near-wall region are sensitive to the measurement environment (background noise

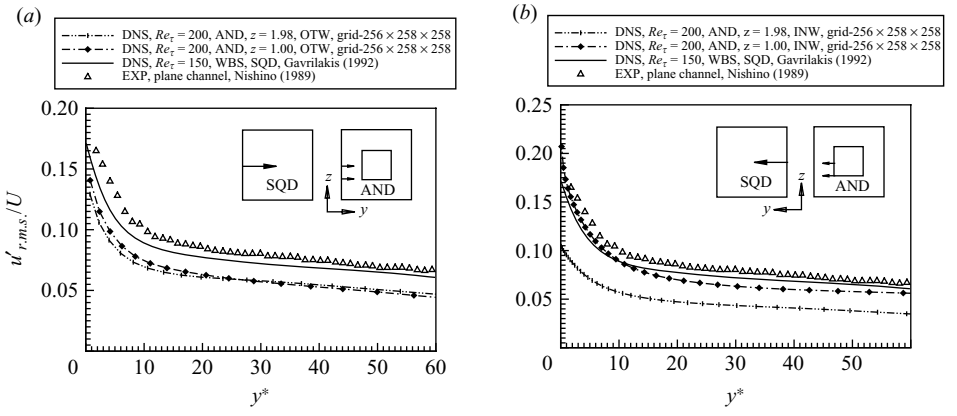

FIGURE 21. Limiting near-wall behaviour of $w'_{r.m.s.}/U$ (*a*) near the outer wall and (*b*) near the inner wall.

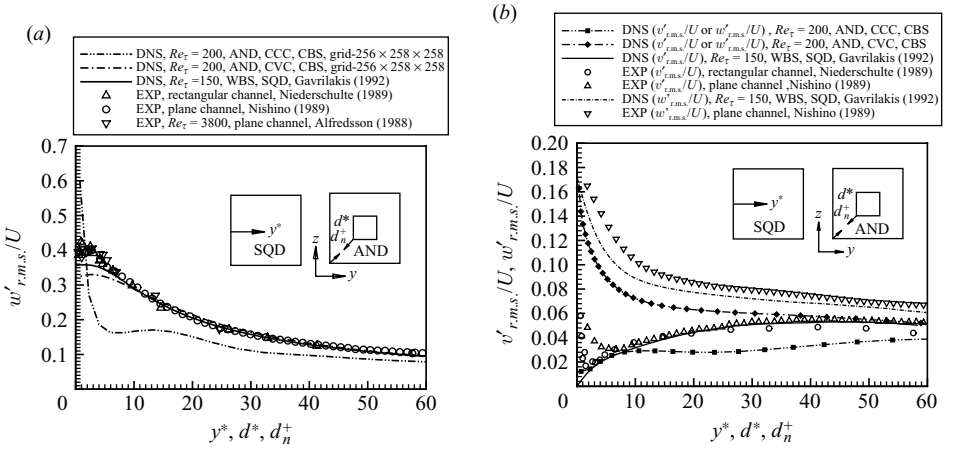

FIGURE 22. Limiting near-corner behaviour of (*a*) $u'_{r.m.s.}/U$, and (*b*) $v'_{r.m.s.}/U$ or $w'_{r.m.s.}/U$ near the concave and convex corners along the corner bisector.

or other disturbances). The $v'_{r.m.s.}/U$ near the inner wall at $z = 1.98$ was similar to that along the wall bisector of the square duct, but the values were lower, as shown in figure 20(*b*). However, the $v'_{r.m.s.}/U$ near the inner wall in the vicinity of the convex corner had a sharp increase. Distributions at other z stations are included in figure 20(*b*) to confirm that the sharp increase was due to the flow geometry (convex-corner tip effects) rather than the numerical sensitivity.

Figure 21 presents the limiting near-wall behaviours of $w'_{r.m.s.}/U$ for the outer and inner walls, respectively. The $w'_{r.m.s.}/U$, from either Gavrilakis (1992) or the current DNS, had similar pattern. An extrapolation performed near the outer wall, shown in Figure 21(*a*), gave $w'_{r.m.s.}/U = 0.167$ at $z = 1.00$ and 0.157 at $z = 1.98$, which were close to the value of 0.170 reported by Gavrilakis (1992) and 0.165 from Nishino & Kasagi (1989). Near the inner wall, as seen in figure 21(*b*), the $w'_{r.m.s.}/U$ is lower (0.106) at $z = 1.98$ and higher (0.206) at $z = 1.00$, which is consistent with the observation in figure 4 that the convex corner generated quite a strong streamwise vorticity (ω_x).

In addition to the wall limiting behaviour, the corner limiting performance of the turbulence intensities would be an interesting subject to interrogate. Figure 22 gives the concave- and convex-corner limiting curves along the corner bisector for the $u'_{r.m.s.}/U$ and $v'_{r.m.s.}/U$ or $w'_{r.m.s.}/U$. The limiting behaviour near the convex corner was similar to the corresponding wall limiting behaviour with the $u'_{r.m.s.}/U$ equal to 0.324 and the $v'_{r.m.s.}/U$ or $w'_{r.m.s.}/U$ equal to 0.162 at the convex-corner tip. However, the limiting value of $u'_{r.m.s.}/U$ was significantly high (0.604) near the concave corner, suggesting that the concave corner provided an effective damping for the mean streamwise velocity, but not as effective for the streamwise turbulence, resulting in a significantly high ratio.

3.2.3. *Origins of turbulence-driven secondary flow*

Since the streamwise vorticity is a key parameter for quantifying the intensity of the secondary flow in a generic straight duct, the mean streamwise vorticity transport equation for fully developed (statistically stationary) turbulence,

$$V\frac{\partial \bar{\Omega}_x}{\partial y} + W\frac{\partial \bar{\Omega}_x}{\partial z} = \nu\left(\frac{\partial^2 \bar{\Omega}_x}{\partial y^2} + \frac{\partial^2 \bar{\Omega}_x}{\partial z^2}\right) + \underbrace{\underbrace{\left(\frac{\partial^2}{\partial y^2} - \frac{\partial^2}{\partial z^2}\right)(-\overline{v'w'})}_{\text{shear stress contribution}} + \underbrace{\frac{\partial^2}{\partial y \partial z}(\overline{v'^2} - \overline{w'^2})}_{\text{normal stress contribution}}}_{SFG(\text{secondary flow generation})}, \qquad (3.2)$$

was applied to study the origins of TDSF in a square duct, in particular near the concave 90° corner, by a number of researchers, including Brundrett & Baines (1964), Gessner & Jones (1965) and Perkins (1970) in their earlier analytical and experimental investigations and Madabushi & Vanka (1991), Gavrilakis (1992) and Huser & Biringen (1993) in their LES/DNS. As an extension of these studies, the current research applied (3.2) to the TDSF in the square annular duct to better understand its formation mechanisms near the convex 90° corner and confirm the flow similarity by comparing the SFG structures near the concave 90° corner to the square duct DNS data.

The mean streamwise vorticity, calculated from the mean TDSF vector field of figure 4, is plotted in figure 23 near the convex and concave corners. With the x-axis pointing out of the figure's planes defined as positive, the vorticity had one positive peak of $\Omega_x = 3.5$ near the concave corner located at $(y, z) = (0.302, 0.118)$ denoted by $\oplus$ in figure 23(a) and another positive peak of $\Omega_x = 7.8$ near the convex corner at $(y, z) = (1.031, 0.854)$ denoted by $\otimes$ in figure 23(b) immediately below the corner bisector. The vorticity peak centre is different from the vortex core that is defined as the zero mean secondary velocity point and is used as the trimming parameter for flow similarity in § 3.1.4. From the positive peak ($\oplus$) near the concave corner, the vorticity decreased as the side wall at $z = 0$ was approached and attained a negative minimum of $\Omega_x = -5.4$ on the wall. The sign of Ω_x changed at $(y, z) = (0.302, 0.053)$, a distance of $z^+ = 10.6$ away from the side wall, whereas this value was $z^+ = 7$ in Gavrilakis (1992). The present Ω_x showed similar structures compared to the DNS of Gavrilakis (1992). The corresponding secondary vortex generation is plotted in figure 24(a). The global peak of the secondary flow generation (SFG) with a value of 10.38 near the concave corner occurred at the location of $(y, z) = (0.240, 0.067)$. Based

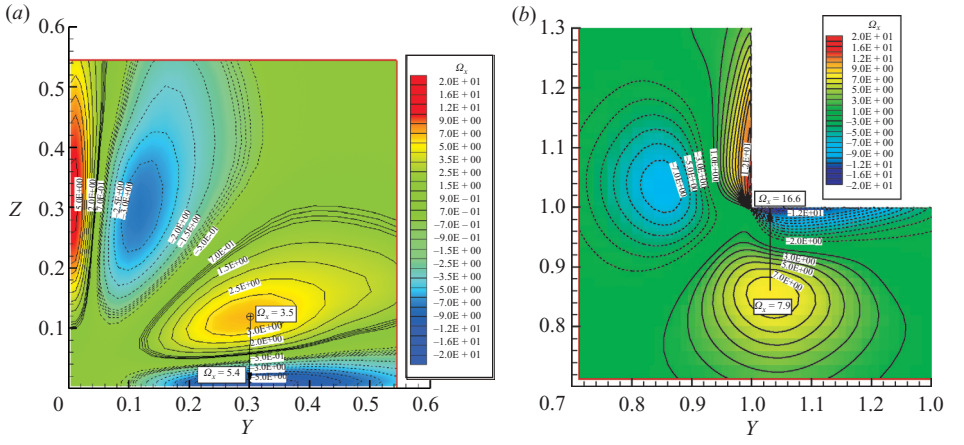

FIGURE 23. Streamwise vorticity (Ω_x) near the (a) concave corner and (b) convex corner.

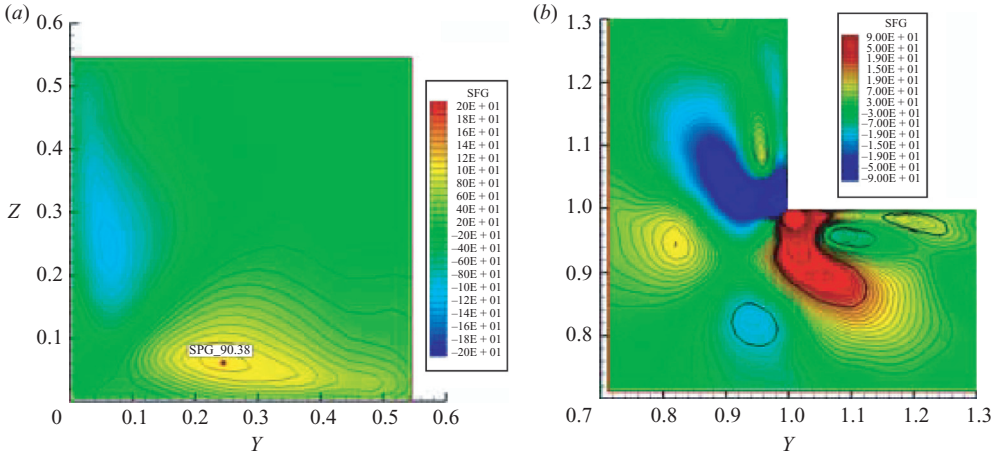

FIGURE 24. 'Stress-induced' SFG near the (a) concave corner and (b) convex corner.

on the flow similarity analysis in § 3.1.4 and the SFG distribution, the area affected by the concave corner for a symmetric corner boundary layer covered a region of $(y, z) = (0–0.5, 0–0.5)$, which is equivalent to a circular area centred at the corner tip with a radius of $d_n^+ = 100$. This conclusion is subject to a precaution due to the influence of the inner side walls and the convex corner, since these boundaries will constraint the growth of the concave corner boundary layer.

Now the attention is switched to the convex corner at which the vorticity structures shown in figure 23(b) presented a qualitatively similar scenario compared to the concave corner. Below the corner bisector, a large vorticity cell with a peak value of $\Omega_x = 7.9$ was located at $(y, z) = (1.031, 0.854)$, which was equivalent to $(y^+, z^+) = (6.26, 29.3)$ away from the convex corner tip. From this peak point, the vorticity decreased as the inner side wall at $z = 1.0$ was approached, reaching a local minimum peak of $\Omega_x = -16.60$ on the inner side wall. However, a global minimum of $\Omega_x = -19.94$ was detected on the inner side wall at $y^+ = 1.4$ away from the corner tip. The sign of the vorticity changed at $(y, z) = (1.031, 0.942)$, a distance of 0.0585 (or equivalent $z^+ = 11.7$) away from the inner side wall. The magnitudes of the

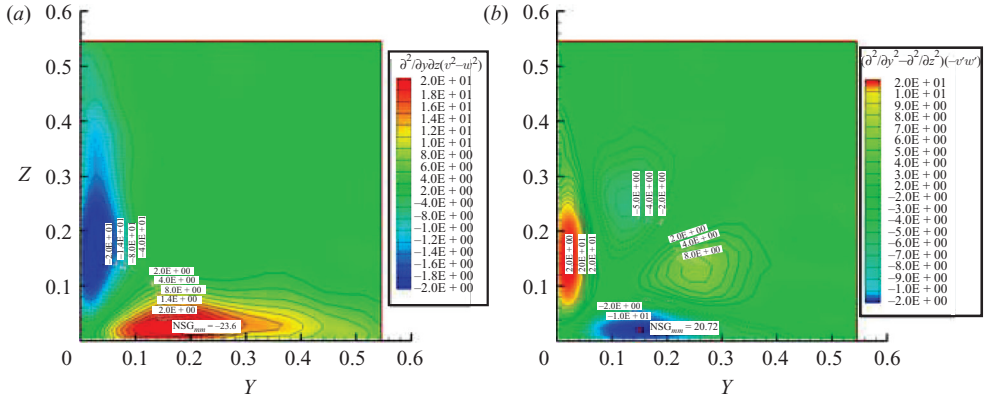

FIGURE 25. 'Stress-induced' SFG near the concave corner (*a*) NSG and (*b*) SSG.

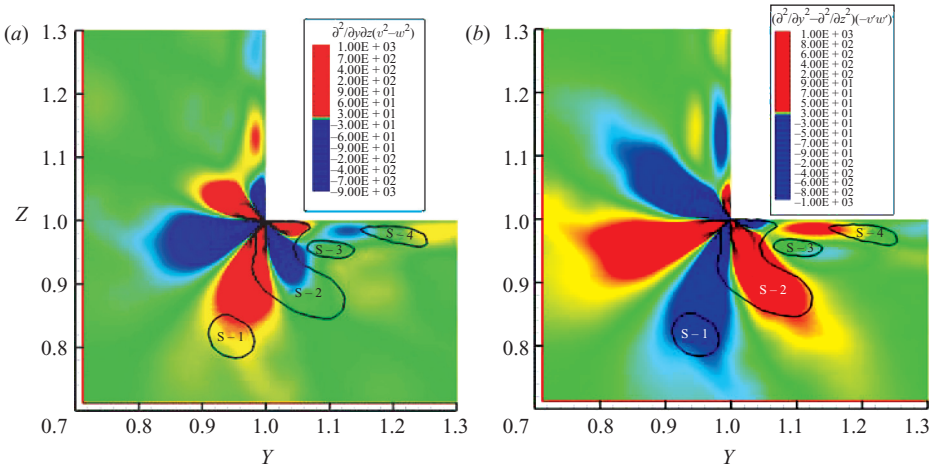

FIGURE 26. 'Stress-induced' SFG near the convex corner (*a*) NSG and (*b*) SSG.

maximum and minimum vorticities were two to four times greater than those near the concave corner. The SFG distribution near the convex corner, as formulated in (3.2), is given in figure 24(*b*). Unlike the concave corner, the distributions exhibited a highly conjugated pattern with alternating positive and negative generation structures both across the corner bisector due to the flow symmetry properties and on one side of the corner bisector due to the vorticity generation mechanisms. The global peak SFG for the convex corner was located at the tip of the corner and had an extremely high value of 2383. This further demonstrates the region affected by the convex corner for a symmetric corner boundary layer roughly covered an area of $(y, z) = (0.7–1.3, 0.7–1.3)$ with the corner tip located at $(y, z) = (1.0, 1.0)$, which is equivalent to an 'L-shaped' region around the corner with the outer boundary a distance of $d_n^+ = 120$ away from the inner side wall and corner tip, as seen in figure 24(*b*). Again, this conclusion is made with a precaution that the actual affected area might be larger due to the constraint effects of the outer side walls and the concave corner.

There have been many debates regarding roles played by the shear and normal stress contributions in the total SFG (see Brundrett & Baines 1964, Gessner & Jones 1965 and Perkins 1970). Most of the arguments have been based on either

experimental or analytical results, near a concave 90° corner. Figure 25 provides the normal stress generation (NSG) and shear stress generation (SSG) near the concave corner. The two production terms were of the same order of magnitude, with $NSG_{max} = 23.6$ and $SSG_{max} = 20.7$, but had opposite signs in the near side wall region. This is in agreement with the observations in Gessner & Jones (1965) and Perkins (1970). Since the net production signs in figure 24(*a*) followed the NSG's signs in figure 25(*a*), the NSG is concluded to be dominant in the near side wall region, whereas the SSG governs the region away from the side wall.

The generation terms of the NSG and SSG near a convex corner exhibited more complex structures with a salient 'butterfly' shape. Both the NSG and SSG 'butterflies' had the three distinctive zones, consisting of the antenna, side wing and tail wing symmetrically located with respect to the corner bisector. In addition, some substructures were identified besides the antenna and side wing near the inner side walls. Although the sizes of the two butterflies had a slight difference when the same color scale applied, they were, indeed, a conjugate pair in the sense that each zone of one butterfly carried the sign opposite to that of the corresponding zone of its counterpart. Based on the net generation (SFG) presented in figure 24(*b*), four major structures, S-1, S-2, S-3 and S-4, on one side of the corner bisector were identified according to their signs or colours, which exhibited an alternate positive and negative arrangement between the inner side wall and the corner bisector. By patching the areas of these structures onto the NSG and SSG in figure 26, the contribution roles of the NSG and SSG can be qualitatively determined. Within S-1, both the NSG and SSG contributions came from the tail-wing zone. Since the SFG in S-1 carried a negative sign that agreed with the SSG sign, the SSG was dominant within S-1. Since the S-2 structure covered part of the tail wing and the side wing, as well as the entire zone of the antenna, and the sign of the SFG was positive, the NSG and SSG alternated dominance within S-2; i.e. the NSG dominated in the tail-wing region, followed by the SSG in the side-wing region and then the NSG in the antenna zone. Following the same reasoning, S-3 was generated by the NGS, and S-4 was generated by the SSG. Since the maximum generations for both the NSG and SSG were produced within a small region almost right at the corner tip, it is deducible that the corner tip, if infinitely sharp in a mathematical or numerical sense, is a singularity point in terms of the SFG. However, the corner tip in reality must have some degree of curvature or sharpness tolerance. The grid refinement, hence, must only be conducted to a certain level until reaching the tolerance requirement.

3.2.4. *Turbulence fluctuation structures*

The instantaneous fluctuation fields are presented in this section to highlight some of the distinctive features of turbulence in the square annular duct. Figure 27(*a*) shows the instantaneous streamwise velocity contours in the lower-left quadrant of one cross-section plane, upon which is superimposed the corresponding secondary velocity vector field. The streamwise velocity contours were characterized by the mushroomlike shapes protruding from both the inner and outer side walls. The associated secondary velocity vectors clearly indicate that these mushroom structures were caused by the sweeps and ejection (or bursts) events. The sweeps brought the higher momentum from the outer turbulent region into the near-wall and near-corner regions, and the bursts transported the low-momentum fluid back to the high-turbulence zones. This essentially formed the mechanisms of the turbulent mixing and transport process. In the streamwise direction, as demonstrated in figure 27(*b*), the flow is characterized

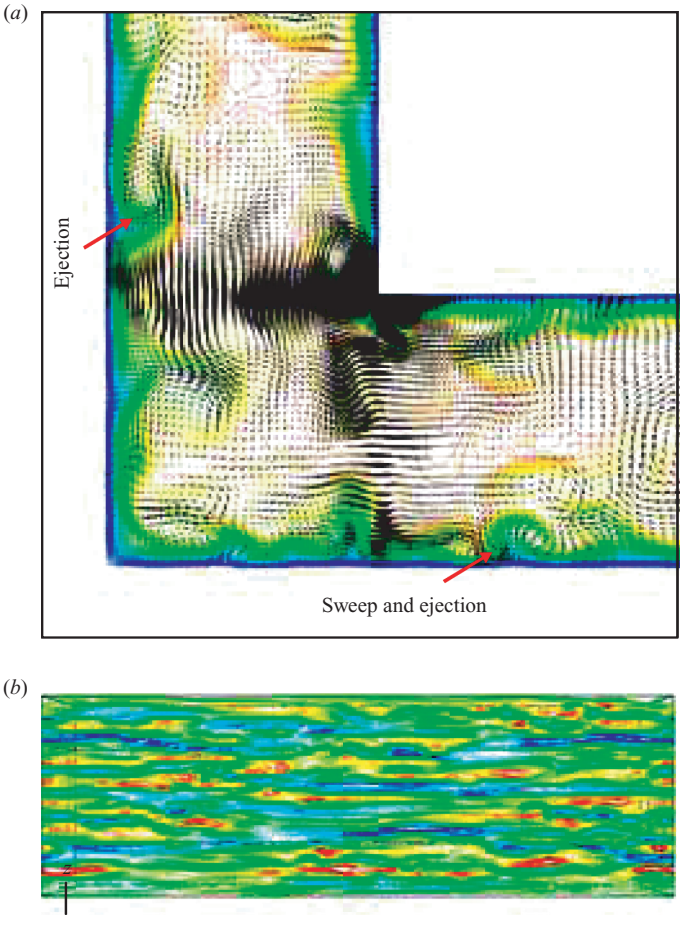

FIGURE 27. (*a*) Instantaneous flow field on a cross-streamwise plane: streamwise velocity contours and secondary velocity vectors; (*b*) instantaneous streamwise velocity fluctuation field on the streamwise plane of $y^+ = 13.4$ near the outer side wall.

by streaky structures in a near-wall plane, which is caused by the wall shear layer effects.

4. Conclusions

DNS results for the fully developed turbulence in a square annular duct were obtained by systematic grid refinement studies, including the preliminary LES run on a grid of $130 \times 66 \times 66$, an LES study using a grid of $130 \times 130 \times 130$ in Xu & Pollard (2001) and ultimately the current DNS with a grid of $256 \times 258 \times 258$. The mean flow field and turbulence statistics, including the Reynolds stresses and turbulence energy spectra, were accumulated in the course of the flow evolution, and these data were verified against a variety of existing turbulence databases. The current DNS exhibited high levels of agreement with the DNS in a square duct from Gavrilakis (1992) and Huser & Biringen (1993) and a broad range of experiments, such as those of Niederschulte (1989), Nishino & Kasagi (1989) and Cheesewright *et al.* (1990), as well as von Karman's 'law-of-the wall' and Kolmogorov's '$-5/3$ law'.

Turbulent boundary layers of the concave and convex 90° corners were identified by studying the near-corner behaviours of the mean streamwise velocity. The concave 90° corner dampened the mean streamwise velocity U^+ near the corner, and U^+ as a function of the normalized corner bisector distance d_n^+ is analytically expressed as $U^+(d_n^+) = d_n^+(1 - e^{-d_n^+/25})$ for $0 \leqslant d_n^+ \leqslant 20$ and $U^+(d_n^+) = 2.5 \ln d_n^+ + 6.5$ for $30 \leqslant d_n^+ \leqslant 100$. The convex 90° corner enhanced the mean streamwise velocity near the corner, and the velocity profiles along corner bisector were curve fitted, using an analytical formulation by introducing the enhancement function: $U^+(d_n^+) = d_n^+(1 + e^{-d_n^+/5})^{u^*/u_\tau}$ for $0 \leqslant d_n^+ \leqslant 10$ and $U^+(d_n^+) = 2.5 \ln(d_n^+) + 8.0$ for $20 \leqslant d_n^+ \leqslant 100$. These formulations reveal that the boundary layer of concave 90° corner is characterized by a zero wall shear stress, and the non-dimensional wall shear stress for the convex 90° corner is at 3.261 based on the current grid resolution.

By comparing the flow patterns near the concave 90° corner in the present study with the DNS data from Gavrilakis (1992) and the experiment from Cheesewright et al. (1990), a flow similarity rule was discovered, and the location of the corner-vortex core was identified as the parameter for trimming the flows so that the flow fields were quantitatively comparable. The flow similarity near a concave 90° corner was validated by comparing the mean streamwise and secondary velocities as well as the turbulence intensities of $u'_{r.m.s.}$ and $w'_{r.m.s.}$. The location of the vortex core for the convex corner was provided for future checks of flow similarity in convex 90° corner turbulence under symmetric mean flow conditions. Based on the 'law-of-the-corner' formulations and the flow similarity properties, we recommend that the 'corner functions', supplementing the 'wall function', be developed, in either an analytical or a tabular form, to improve the accuracy of RANS simulations.

The limiting behaviours of the turbulence intensities near the wall and corners were studied and compared with the existing experiment and DNS. The limiting behaviours of these intensities near the convex corner were found quite similar to that near a flat plate, whereas the limiting behaviours near the concave corner differed. A rescaling study of the turbulence shear stresses concluded that the streamwise shear stress $\overline{u'v'}$ and the cross-streamwise shear stress $\overline{v'w'}$ must be rescaled by $u'_{r.m.s.}v'_{r.m.s.}$ and $v'_{r.m.s.}w'_{r.m.s.}$, respectively, so that their distributions and magnitudes become more universal and normalized. The current investigation demonstrated the importance of these scaling laws in the vicinity of the corner regions, and the turbulence scaling laws at higher Reynolds numbers are the points of interest that warrant a further investigation in future.

A TES analysis was conducted based on the DNS data in the square annular duct. The anisotropy properties of the turbulence motions at different scales led to re-evaluation of the validity of the conventional turbulence eddy viscosity concept. To address the anisotropy motions in turbulence correctly, a tensor form of turbulence eddy viscosity is recommended in the future development of RANS turbulence closure models and LES subgrid scale models.

The TDSF in the square annular duct was predicted as a chain of strong, counter-rotating vortex pairs symmetrically located around the convex 90° corner and a weak counter-rotating vortex pair symmetrically located around the concave 90° corner. By interrogating the origin of these secondary flows, prominent butterfly structures were identified for the normal and shear stress contributions near the convex corner. The normal and shear stress contributions were conjugate to each other, and they alternated dominance in different zones near the convex corner.

The current investigation revealed in-depth knowledge of the corner turbulence physics and provided a solid validation for the N-S equation solution technology

developed in Xu *et al.* (2005). This simulation technique opens the door to use LES/DNS to directly attack the turbulence in generic Cartesian geometries, such as rectangular ducts and rectangular annular channels. The extension of this technology to more general complex geometry turbulent flows will be a major task in future.

The research originated from the PhD research of Dr Xu, supervised by Professor Andrew Pollard at Queen's University of Canada. The author would like to thank Dr Gavrilakis, Dr Huser and Dr Biringen for providing their DNS results to validate the current investigation. Thanks are also due to Dr Stuart McIlwain, Dr Norman Ball and Dr Steve Zan at the Institute for Aerospace Research (IAR), National Research Council (NRC), of Canada for their constructive discussions and reviews of the current work.

REFERENCES

Alfredsson, P. H., Johansson A. V., Haritonidis J. H. & Eckelmann, H. 1988 The fluctuating wall shear stress and the velocity field in the viscous sublayer. *Phys. Fluids* **31**, 1026–1033.

Bradshaw P. 1987 Turbulent secondary flows. *Annu. Rev. Fluid Mech.* **19**, 53–74.

Breuer M. & Rodi W. 1994 Large eddy simulation of turbulent flow through straight and curved ducts. *ERCOFTAC Bulletin* **22**, 26–29.

Brundrett E. & Baines W. D. 1964 The production and diffusion of vorticity in duct flow. *J. Fluid Mech.* **19**, 375–394.

Cheesewright R., McGrath G. & Petty D. G. 1990 LDA measurements of turbulent flow in a duct of square cross section at low Reynolds number. *Tech Rep.* 1011. Aeronautical Engineering Department, Queen May Westfield College, University of London.

Choi H., Moin P. & Kim, J. 1993 Direct numerical simulation of turbulent flow over riblets. *J. Fluid Mech.* **255**, 503–539.

Demuren A. O. & Rodi W. 1984 Calculation of turbulence-driven secondary motion in non-circular ducts. *J. Fluid Mech.* **140**, 189–222.

van Driest E. R. 1956 Turbulent flow near a wall. *J. Aeronaut. Sci.* **23**, 1007–1011.

Gavrilakis S. 1992 Numerical simulation of low-Reynolds-number turbulent flow through a straight square duct. *J. Fluid Mech.* **244**, 101–129.

Gessner F. B. & Jones J. B. 1965 On some aspects of fully developed turbulent flow in rectangular channels. *J. Fluid Mech.* **23**, 689.

Hartnett J. P., Koh J. C. Y & McComas S. T. 1962 A comparison of predicted and measured friction factor for turbulent flow through rectangular duct. *Trans. ASMEC: J. Heat Transfer* **84**, 82.

Huser A. & Biringen S. 1993 Direct numerical simulation of turbulent flow in a square duct. *J. Fluid Mech.* **257**, 65–95.

Kajishima T. & Miyake Y. 1992 A discussion on eddy viscosity models on the basis of the large eddy simulation of turbulent flow in a square duct. *Comp. Fluids* **21**, 151–161.

von Karman Th. 1930 Mechanische Ahnlichkeit und Turbulenz. In *Proc. 3rd Intl Cong. on Applied Mechanics*, Stockholm.

Kim J. & Moin P. 1985 Application of a fractional-step method to incompressible Navier–Stokes equations. *J. Comp. Phys.* **59**, 308–323.

Kim J., Moin P. & Moser R. 1987 Turbulence statistics in fully developed channel flow at low Reynolds number. *J. Fluid Mech.* **177**, 133–166.

Kolmogorov A. N. 1942 The equation of turbulent motion in an incompressible viscous fluid. *Izv. Akad. Nauk S.S.S.R. Ser. Fiz.* **6**, 56–58.

Kolmogorov A. N. 1962 A refinement of previous hypotheses concerning the local structure of turbulence in a viscous imcompressible fluid a high Reynolds number. *J. Fluid Mech.* **12**, 82–85.

Kreplin H. P. & Eckelmann H. 1979 Behavior of the three fluctuating velocity components in the wall region of a turbulent channel flow. *Phys. Fluids* **22**, 1233–1239.

Launder B. E. & Ying W. M. 1973 Prediction of flow and heat transfer in ducts of square cross-section. *Proc. Inst. Mech. Engng* **187**, 455.

Madabhushi R. K. & Vanka S. P. 1991 Large eddy simulation of turbulence-driven secondary flow in a square duct. *Phys. Fluids* A **3**(11), 2734–2745.

Niederschulte M. A. 1989 Turbulent flow through a rectangular channel. PhD thesis, University of Illinois at Urbana-Champaign, IL, USA.

Nikuradse J. 1930 Turbulente stromung in nicht-kreisformigen Rohren. *Ing. Arch.* **1**, 306–332.

Nishino K. & Kasagi N. 1989 Turbulence statistics measurement in a two-dimensional channel flow using a three-dimensional particle tracking velocimeter. In *Seventh Symp. on Turbulent Shear Flows*, Stanford University, Palo Alto, California.

Perkins, H. J. 1970 The formation of streamwise vorticity in turbulent flow. *J. Fluid Mech.* **44**, 721.

Prandtl L. 1904 Motion of fluids with very little viscosity. National Advisory Committee for Aeronautics, Technical Memorandum No. 452, pp. 484–491.

Prandtl L. 1926 Uber die ausgebildete turbulenz. Verh. In *2nd Intl Kong. Fur Tech. Mech.*, Zurich..

Rai M. M. & Moin P. 1991 Direct simulation of turbulent flow using finite difference schemes. *J. Comp. Phy.* **96**, 15.

Reynolds O. 1883 An experimental investigation of the circumstances which determine whether the motion of water shall be direct and sinuous and the law of resistance in parallel channels. *Phil. Trans. R. Soc. Lond.* 51–105.

Speziale C. G. 1987 On nonlinear k–l and k–ε models of turbulence. *J. Fluid Mech.* **178**, 459–475.

Wang Jiasheng 1982 Tensor Analyses and Applications. Shanghai Institute of Mechanical Engineering.

Warsi Z. U. A. 1993 *Fluid Dynamics: Theoretical and Computational Approaches*. CRC Press.

Wesseling P. 2001 *Principles of Computational Fluid Dynamics*. Springer.

Xu H. & Pollard A. 2001 Large eddy simulation of turbulent flows in a square annular duct. *Physics of Fluids* **13** (11), 3321–3337.

Xu H., Yuan W. & Khalid M. 2005 Design of a high-performance unsteady Navier–Stokes solver using flexible-cycle additive-correction multi-grid technique. *J. Comp. Phys.* **209**, 504–540.